Supplementary Materials for

# Boosting Hydrogen Evolution Activity: Next-Nearest Oxygen Coordination in Dual-Phase Supra-Nanostructured Multiprincipal Element Alloy Catalysts

Fucong Lyu[1,2,3], Chang Liu[4], Shanshan Zeng[1], Xiuming Bu[5], Yuhan Chen[2,9], Zhe Jia[6,9], Youneng Xie[2,9], Ligang Sun[7,9,*], Zhengyi Mao[2,9], Junda Shen[1], Gan Li[2,9], Juanhua Luan[9], Yang Yan[2,9], Lu Yao[2,9], Lanxi Li[2,9], Xianying Wang[5], Ge Wu[8], Yang Yang Li[1], and Jian Lu[1,2,3,9,10,*]

*[1] Department of Material Science and Engineering, City University of Hong Kong, 83 Tat Chee Avenue, Kowloon, Hong Kong, China*
*[2] Centre for Advanced Structural Materials, City University of Hong Kong Shenzhen Research Institute, Greater Bay Joint Division, Shenyang National Laboratory for Materials Science, Shenzhen 518057, China*
*[3] Hong Kong Branch of National Precious Metals Material Engineering Research Centre, City University of Hong Kong, 83 Tat Chee Avenue, Kowloon, Hong Kong, China*
*[4] Center for Alloy Innovation and Design (CAID), State Key Laboratory for Mechanical Behavior of Materials, Xi'an Jiaotong University, 710049 Xi'an, China*
*[5] CAS Key Laboratory of Materials for Energy Conversion, Shanghai Institute of Ceramics, Chinese Academy of Sciences (SICCAS), Shanghai 200050, P.R. China*
*[6] School of Materials Science and Engineering, Southeast University, Nanjing 211189, China*
*[7] School of Science, Harbin Institute of Technology, Shenzhen 518055, China*
*[8] Center for Advancing Materials Performance from the Nanoscale (CAMP-Nano) and Hysitron Applied Research Center in China (HARCC), State Key Laboratory for Mechanical Behavior of Materials, Xi'an Jiaotong University, 710049 Xi'an, China*
*[9] Department of Mechanical Engineering, City University of Hong Kong, 83 Tat Chee Avenue, Kowloon, Hong Kong, China*
*[10] City University of Hong Kong Matter Science Research Institute (Futian), Shenzhen 518045, China*

***Corresponding authors. Email: jianlu@cityu.edu.hk (J.L.)**

**This PDF file includes:**

## Materials and methods

**Materials:** Raw element granules of aluminium (Al), zinc (Zn), titanium (Ti), zirconium (Zr), silicon (Si), copper (Cu), and nickel (Ni) with a purity higher than 99.95% were mixed by China Material Technology Co., Ltd to achieve the high-entropy amorphous alloy (HEAA) sputtering target with a theoretical atomic composition (at%) of $Al_{0.5}ZnTiZrSiCuNi$. The pure palladium (Pd) target with a purity higher than 99.99% was purchased from Angstrom Engineering Inc. Co., Ltd. Analytical grade potassium hydroxide (KOH), and absolute ethanol were supplied by Sigma Aldrich. All of the solutions were prepared with Milli-Q water (18.2 MΩ cm).

**Materials preparation:** The fabrication method used in this work was magnetron co-sputtering (Angstrom Engineering Inc. Co., Ltd). The background vacuum was $4 \times 10^{-7}$ Torr. HEAA and Pd targets were used for co-sputtering. A supra-nano dual-phase glass-crystal film (denoted SNDP-Pd@HEAA) was then deposited on different substrates (Si(001), carbon cloth, and nickel foam, Pt foil) simultaneously for different purposes. The thickness of the films was easily controlled by the sputtering time and the composition of the films was controlled by tuning the difference in substrate-to-target distances. During this co-sputtering process, the power supplied to the HEAA target with a direct-current source was set at 135 W; the power supplied to the Pd target with a radio-frequency source was set at 105 W; the flow velocity of Ar was 20 sccm and that of $O_2$ was 1 sccm; the chamber pressure was 3 mTorr; the deposition rate was approximately 6 nm $min^{-1}$; and the temperature of the substrate was below 50 °C. The samples obtained at the same condition except in introducing during the synthetic process were denoted as As-SNDP-Pd@HEAA. The pure HEAA film and pure Pd film were prepared by single-target sputtering under the same conditions. For comparison, the samples with different contents of oxygen were prepared under different flow velocities of $O_2$.

**Materials characterisation:** The samples were characterised through scanning electron microscopy (SEM, Philips XL-30 FESEM), atomic force microscopy (AFM, Bruker Icon), and high-resolution transmission electron microscopy (TEM, JEOL TEM 2100F FEG operated with an accelerating voltage of 200 kV). Atomic-resolution scanning transmission electron microscopy (STEM) images and energy-dispersive spectrometry (EDS) maps were acquired on a Titan FEI Themis G60-300 S/TEM (fitted with a high-brightness field emission gun (X-FEG), probe CS corrector, and super-X EDS with four windowless silicon drift detectors). X-ray diffraction (XRD) patterns were collected using an X-ray diffractometer (Rigaku SmartLab) with Cu Kα radiation (λ = 1.5418 Å). Three-dimensional atomic probe tomography (APT) characterisation was performed using a local electrode atom probe (CAMECA LEAP 5000 XR). The APT experiments were conducted at 60 K in laser mode with a laser energy of 50 pJ and a pulse rate of 125 kHz, and the

detection rate was 0.3%. The corresponding three-dimensional reconstructions and data analysis were performed using Imago Visualization and Analysis Software (IVAS, version 3.8.2). Both TEM and APT specimens were prepared on an FEI focused ion beam/scanning electron microscope (FIB/SEM) adopting the lift-out and annular milling method. In the preparation of stability-tested TEM and APT specimens, SNDP-Pd@HEAA was sputtered on nickel foam. The leached metallic ions in the stability test were measured through inductively coupled plasma–optical emission spectrometry (ICP-OES) (Optima ICP-OES Spectrometer, PerkinElmer) with a 10-times diluted solution. (The results were corrected with the dilution factor.) X-ray photoelectron microscopy was performed on an ESCALAB 250 photoelectron spectrometer (ThermoFisher Scientific) with Al Ka (1486.6 eV) as the X-ray source set at 150 W and a pass energy of 30 eV for high-resolution scanning. The base pressure was $3 \times 10^{-9}$ mbar, and the binding energies were referenced to the C1s line at 284.8 eV from adventitious carbon.

The X-ray absorption near edge structure and extended X-ray absorption fine structure experiments on the SNDP-Pd@HEAA catalysts were carried out at the BL14W1 beamline of the Shanghai Synchrotron Radiation Facility. The data were collected in fluorescence mode using a Lytle detector while the corresponding reference sample was measured in transmission mode. The incident beam was monochromatised using a Si (111) fixed-exit, double-crystal monochromator, and a harmonic rejection mirror was applied to cut off the high-order harmonics. The obtained X-ray absorption fine structure data were processed in Athena (version 0.9.26) for background, pre-edge line, and post-edge line calibrations. Fourier transformed fitting was then carried out in Artemis (version 0.9.26). Adopting a $k^3$ weighting scheme, a $k$-range of 3–14 $Å^{-1}$ and an $R$ range of 1 to ~3 Å were used in the fitting for the Pd foil and a $k$-range of 3–11 $Å^{-1}$ and an $R$ range of 1 to ~3.5 Å were used in the fitting for the SNDP-Pd@HEAA samples. Three parameters, the coordination number, bond length, and $E_0$ shift ($CN$, $R$, $\Delta E_0$), were freely fitted for a set Debye–Waller factor $\sigma^2$. In the wavelet transform analysis, $\chi(k)$ exported from Athena was imported into Hama Fortran code. The parameters were an $R$ range of 0–4 Å, a $k$-range of 0–11 $Å^{-1}$ for Pd, and a $k$-weight of 3. A Morlet function with $\kappa = 10$ and $\sigma = 1$ was used as the mother wavelet to give the overall distribution.

**Electrochemical measurements:** The SNDP-Pd@HEAA film was deposited on carbon cloth and glassy carbon electrode (Φ4mm) with a thickness of approximately 350 nm for electrochemical investigation. Electrochemical measurements were conducted in 1.0 M KOH solution at room temperature on a CHI660e electrochemical station with a three-electrode cell system. SNDP-Pd@HEAA, a Hg/HgO electrode, and a graphite rod were used as the working, reference, and counter electrodes, respectively.

To more precisely measure the intrinsic overpotential of the deposited films, linear sweep voltammetry (LSV) for the samples deposited on glassy carbon electrode was recorded at a scan

rate of 5 mV $s^{-1}$ to obtain the polarisation curves. Electrochemical impedance spectroscopy (EIS) was carried out from 100 kHz to 0.1 Hz. A series of cyclic voltammograms were obtained in the potential range of 0–0.1 V (vs. RHE) with scan rates ranging from 10 to 80 mV $s^{-1}$ at non-faradaic overpotentials to demonstrate the current charging and discharging capacitance in estimating the double-layer capacitance ($C_{dl}$). The electrochemical surface area was obtained as $C_{dl}/C_s$, where $C_{dl}$ is the measured double-layer capacitance and $C_s$ is the specific capacitance. In this work, we assumed a $C_s$ value of 0.04 mF $cm^{-2}$ owing to the flat surface of the sample. Long-term stability tests for samples on carbon cloth were performed by continuously applying a current density of 20 and 200 mA $cm^{-2}$ to the working electrode adopting a chronoamperometry method without iR loss correction. The current density was calculated from the geometric surface areas. All of the data presented were corrected for iR losses (taking the generation of gas can increase the ohmic resistance of the liquid electrolyte into account, the resistance R could be measured at the overpotential of -0.1 V versus RHE, with a compensation rate of 90%) and background current, and the potentials were later converted to the reversible hydrogen electrode (RHE) scale.

**AEM electrolyser test:** SNDP-Pd@HEAA on carbon felt and SNDP-Ir@HEAA on porous Ti sheet were used as both cathode and anode catalytic materials. S-type Ti current collectors with a serpentine flow field provided electric conduction and electrolyte transmission. For the cathode or anode compartment, the AEM electrolyser was assembled in the sequence of the end plate, sealing gasket, SNDP-Pd@HEAA/SNDP-Ir@HEAA, and sealing gasket. The geometric area of the SNDP-Pd@HEAA was 1 $cm^2$. An anion-exchange membrane (Sustainion X37-50 Grade T) separated the cathode and anode compartments of the electrolyser. During the tests, 1.0 M KOH electrolyte was fed to both sides of the electrolyser at a rate of 3.5 ml $min^{-1}$ under the control of a peristaltic pump.

**RHE calibration:** All of the potentials reported in this article were calibrated and converted to the RHE scale. The calibration was performed in a high-purity hydrogen-saturated electrolyte with a Pt wire and carbon rod as the working electrode and counter electrode, respectively. We used Hg/HgO electrode as the reference electrode in 1 M KOH. The CV were measured at a scan rate of 1 mV $s^{-1}$. The average of the two potentials at which the current reached zero was taken as the thermodynamic potential for the hydrogen electrode reactions.
In 1 M KOH:

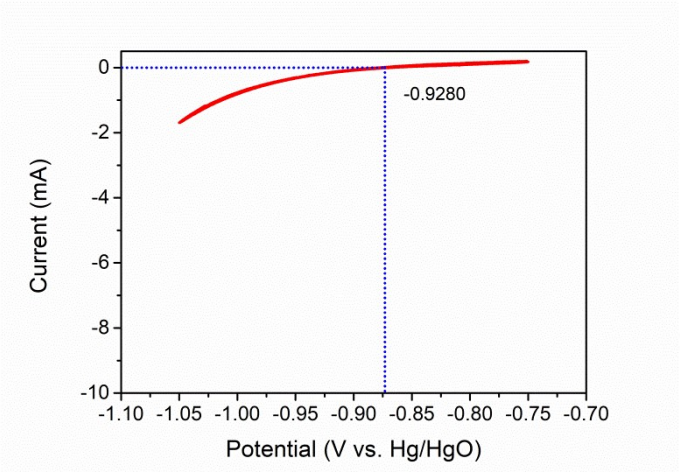


Therefore, in 1 M KOH, $E_{RHE} = E_{Hg/HgO} + 0.9280$.

**DFT calculations**

Density functional theory (DFT) calculations were performed using the Cambridge Sequential Total Energy Package (CASTEP) module in Materials Studio[1]. The generalised gradient approximation method with the Perdew–Burke–Ernzerh function (GGA-PBE) was used to describe the exchange and corrections of atomic interactions[2] and the ultrasoft pseudo-potential method was used to describe the interactions between valence electrons and ionic cores[3]. A plane-wave basis set with a cutoff energy of 400 eV was assigned. The Brillouin zone was sampled using a Monkhorst–Pack grid for the crystal model and a Γ point for the amorphous and crystalline/amorphous interface models[4]. The tolerances of energy, force, and displacement for structural optimisation were $1.0 \times 10^{-6}$ eV/atom, 0.02 eV/Å, and 0.001 Å, respectively. The self-consistent field was set at $1.0 \times 10^{-5}$ eV/atom. The $H_2O$ adsorption energies ($\Delta E_{H2O}$) at the surface of catalysts were calculated according to

$$\Delta E_{H_2O} = E_{surf+H_2O} - E_{surf} - E_{H_2O}$$

where $E_{surf}$ and $E_{surf+H_2O}$ are the total energies of the surface before and after $H_2O$ adsorption. $E_{H_2O}$ represents the energy of a free water molecule.

The Gibbs free energies for hydrogen adsorption ($\Delta G_{H*}$) were calculated according to

$$\Delta G_{H^*} = \Delta E_{H^*} + \Delta ZPE - T\Delta S$$

where $\Delta E_{H^*}$, $\Delta ZPE$, $T$, and $\Delta S$ are the binding energy, zero-point energy change, temperature, and entropy change of the H* adsorption system, respectively.

The vibrational entropy of H* in the adsorbed state is generally negligible. $\Delta S$ was thus calculated as

$$\Delta S = S_{H^*} - \frac{1}{2}S_{H_2} \approx -\frac{1}{2}S_{H_2}$$

where $S_{H_2}$ is the entropy of the gas phase $H_2$ under standard conditions.

Moreover, $\Delta ZPE$ was calculated as

$$\Delta ZPE = ZPE_{H^*} - \frac{1}{2} ZPE_{H_2}$$

Hence, the Gibbs free energy of the adsorbed state of H* was calculated using the simplified equation[5]

$$\Delta G_{H^*} = \Delta E_{H^*} + 0.24\ eV$$

A series of atomistic models were built to study the $H_2O$ adsorption energies and the Gibbs free energies of H* for various active sites in different regions of HEAA samples with and without elemental O. The modelling was consistent with our experimental results. Specifically, three representative models with crystal, amorphous, and crystalline/amorphous dual-phase structures (referred to as Crystal, MG and Interface, respectively) were constructed. To reveal the effect of O addition on the hydrogen evolution reaction performance, three other models with crystal, amorphous, and dual crystalline/amorphous phase structures were constructed with O addition. The specific number and percentage of different elements in the crystal ('Crystal' and 'Crystal-O') and amorphous ('MG' and 'MG-O') models are presented in Supplementary Table 8. The 'Interface' and 'Interface-O' models are obtained from the combination of 'Crystal & MG' and 'Crystal-O' & 'MG-O' models, respectively. To obtain reliable configurations of the amorphous models, first, all atoms were randomly assigned into cubic supercells and periodic boundary conditions were applied in three directions. The amorphous models were then well relaxed and optimised to remove artificial factors. The crystalline/amorphous interface models were built by combining the crystal and amorphous models followed by further relaxation and optimisation. Using the optimised crystal, amorphous, and interface models established above, a vacuum gap ~15 Å wide was introduced to investigate the hydrogen evolution reaction performance of various active sites on the surfaces of these models. Hence, the $H_2O$ adsorption energies and H* Gibbs free energies of six representative models (crystal, amorphous, and interface models with and without O addition) could be investigated to unveil the atomistic mechanism that accounts for the improved hydrogen evolution reaction performance of our catalyst.

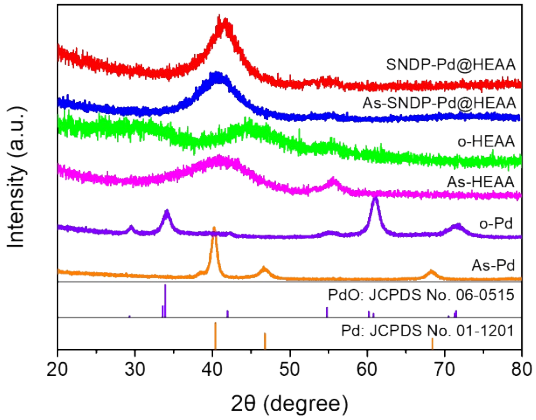


Supplementary Fig. 1 XRD patterns of SNDP-Pd@HEAA, as-SNDP-Pd@HEAA, o-HEAA, As-HEAA, o-Pd, and As-Pd.

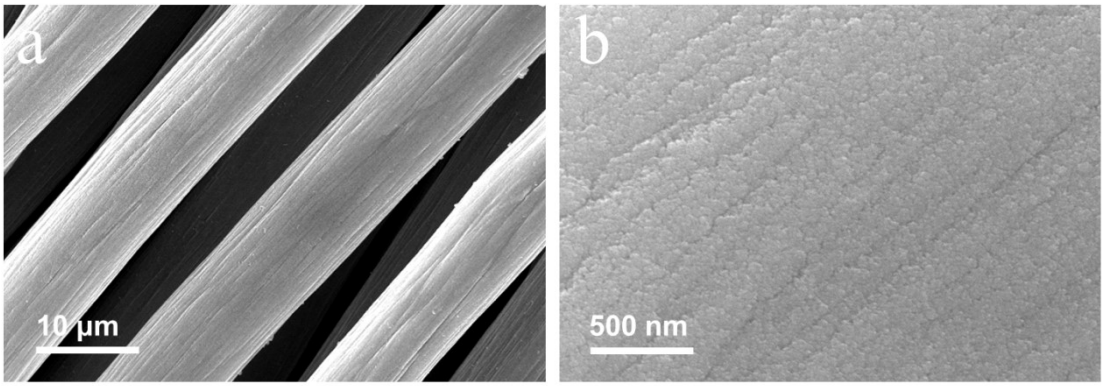


Supplementary Fig. 2 Scanning electron microscopy of SNDP-Pd@HEAA on carbon cloth.

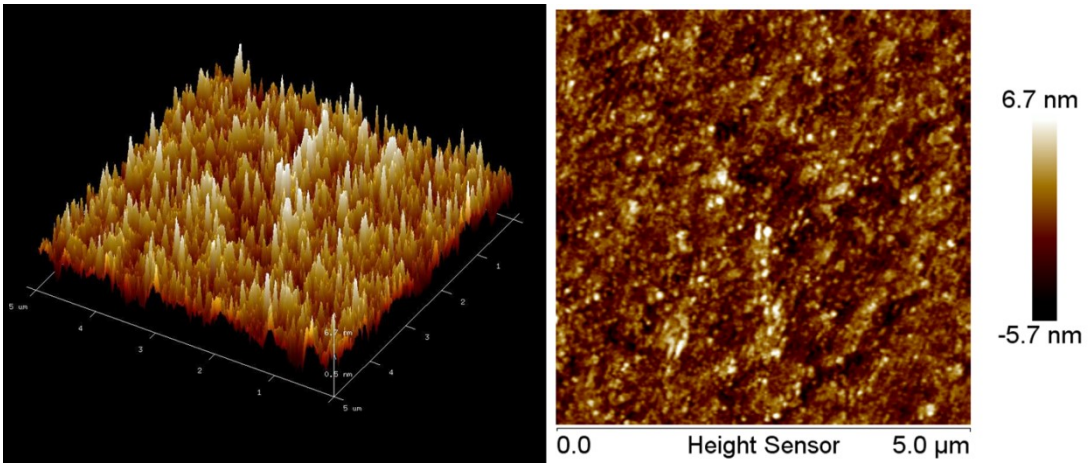


Supplementary Fig. 3 Atomic force microscopy of SNDP-Pd@HEAA.

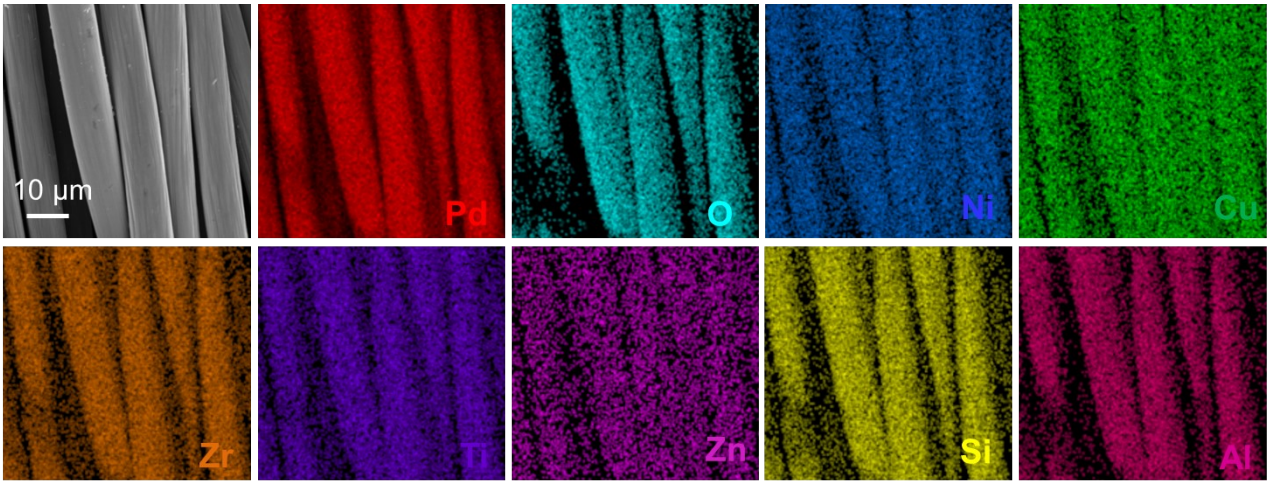


Supplementary Fig. 4 SEM energy-dispersive spectroscopy (EDS) mapping of SNDP-Pd@HEAA.

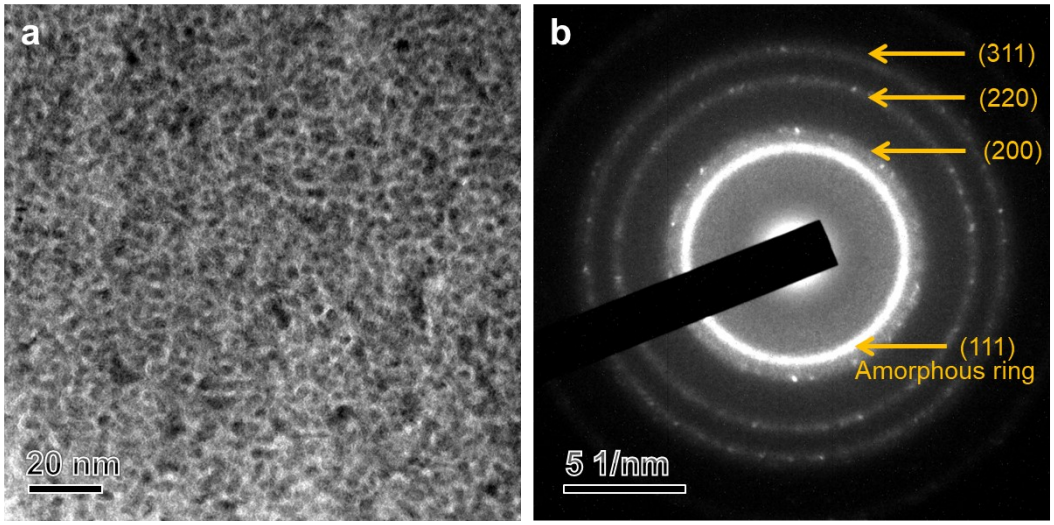


Supplementary Fig. 5 (a) Low-magnification transmission electron microscopy and (b) the corresponding selected area electron diffraction pattern of SNDP-Pd@HEAA.

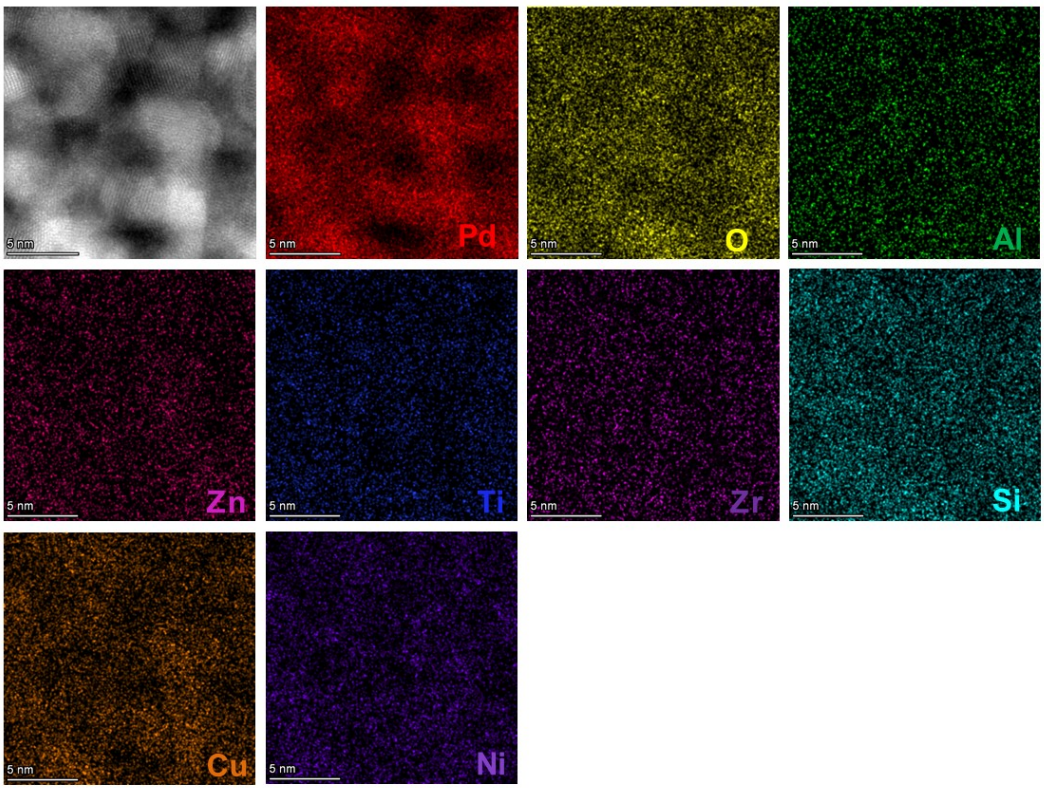


Supplementary Fig. 6 High-angle annular dark-field scanning transmission electron microscopy (HAADF-STEM) image and the corresponding EDS elemental mapping of Pd (red), O (yellow), Al (green), Zn (pink), Ti (blue), Zr (violet), Si (cyan), Cu (orange), and Ni (purple) for SNDP-Pd@HEAA.

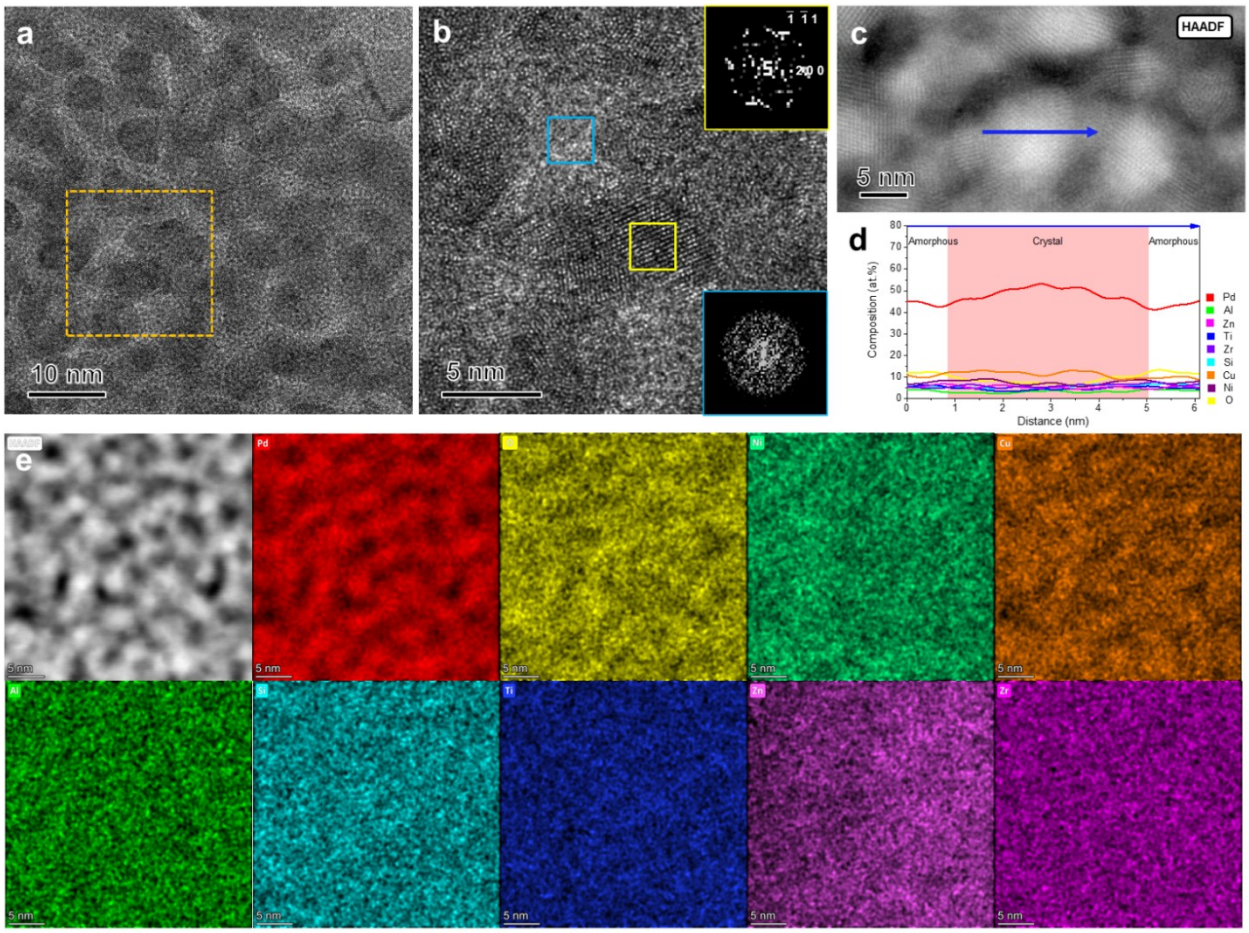


Supplementary Fig. 7 (a) High-magnification TEM and (b) high-resolution TEM (HRTEM). The insets present corresponding fast Fourier transform images showing that the crystal phase has a face-centred cubic structure and the amorphous phase presents a typical diffused ring feature. (c) Typical HAADF-STEM image. The arrow shows the line scan direction of the EDS. (d) Intensity of EDS line scan elements along the arrow in (c). (e) HAADF-STEM image and the corresponding EDS elemental mapping of Pd (red), O (yellow), Al (green), Zn (pink), Ti (blue), Zr (violet), Si (cyan), Cu (orange), and Ni (purple) for As-SNDP-Pd@HEAA.

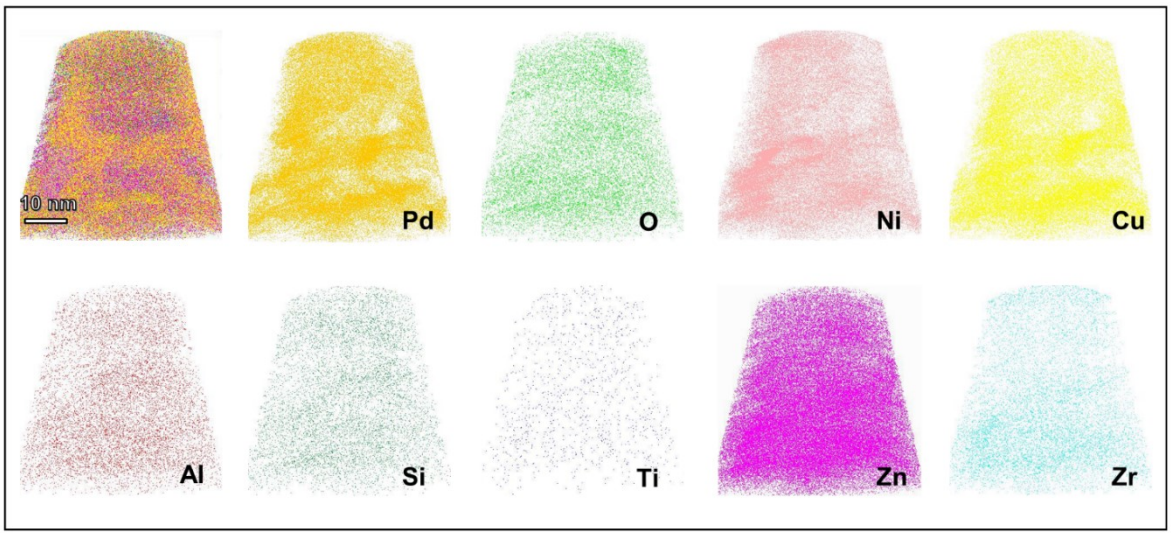


Supplementary Fig. 8 Three-dimensional atomic probe tomography of As-SNDP-Pd@HEAA showing the elemental distribution and multicomponent nature.

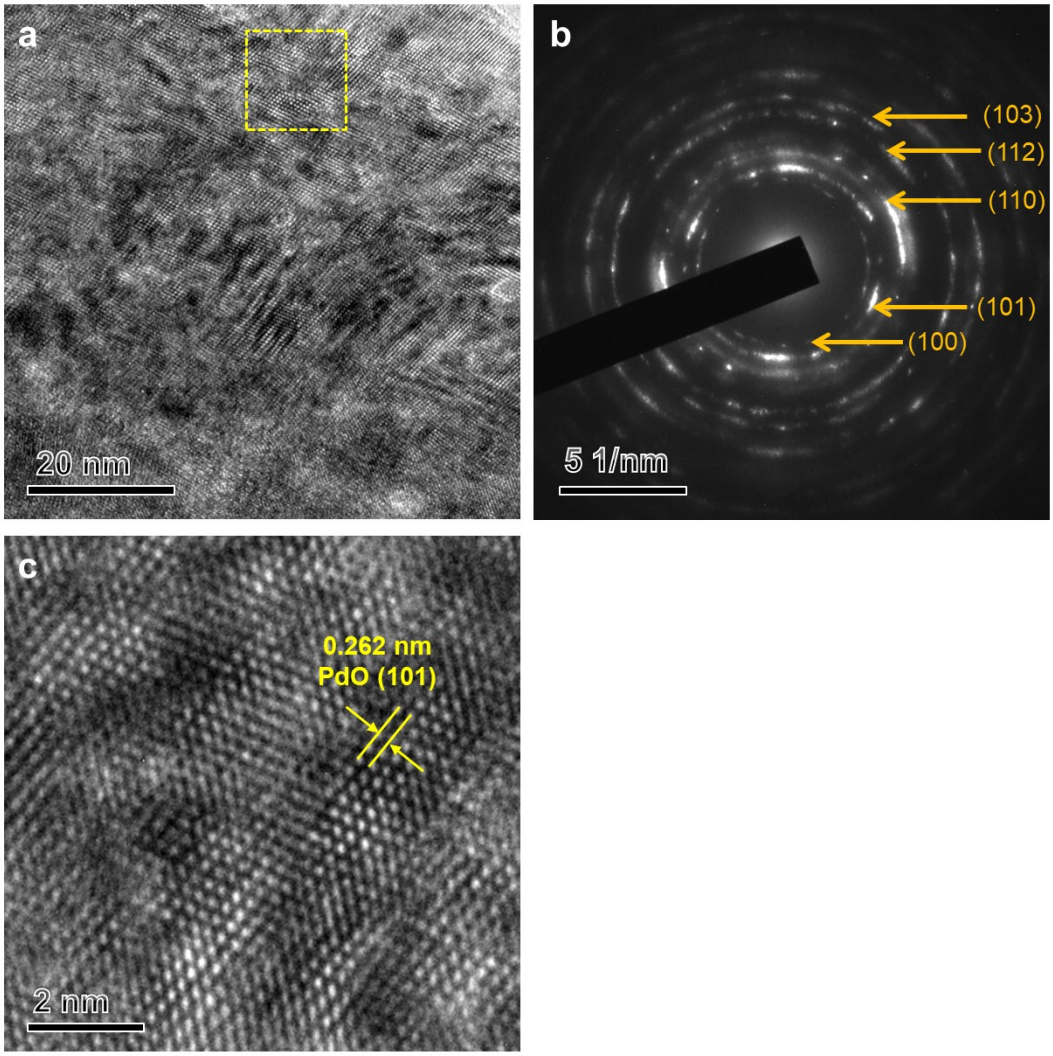


Supplementary Fig. 9 (a) High-magnification TEM, (b) corresponding SAED pattern, and (c) HRTEM of o-Pd.

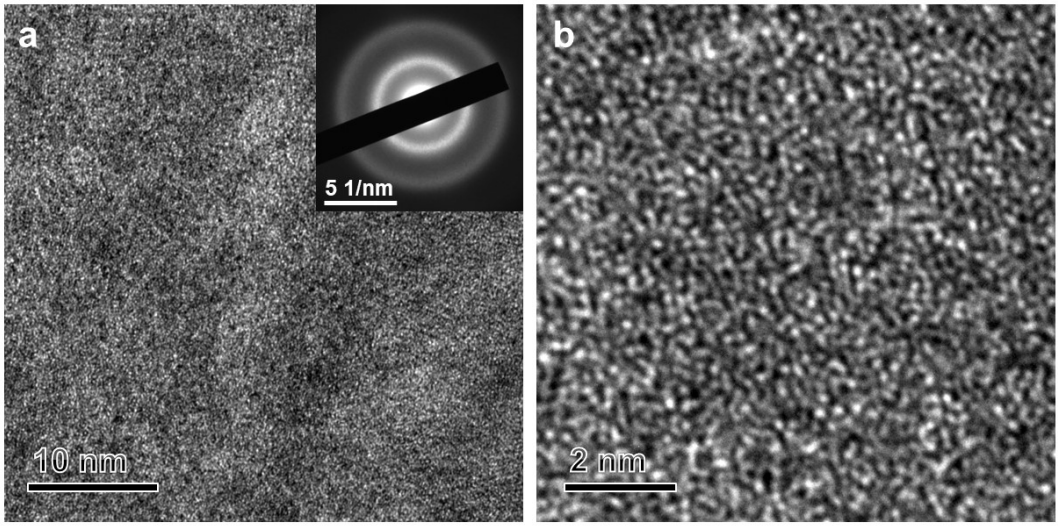


Supplementary Fig. 10 (a) High-magnification TEM, with the inset showing the corresponding SAED pattern, and (b) HRTEM of o-HEAA.

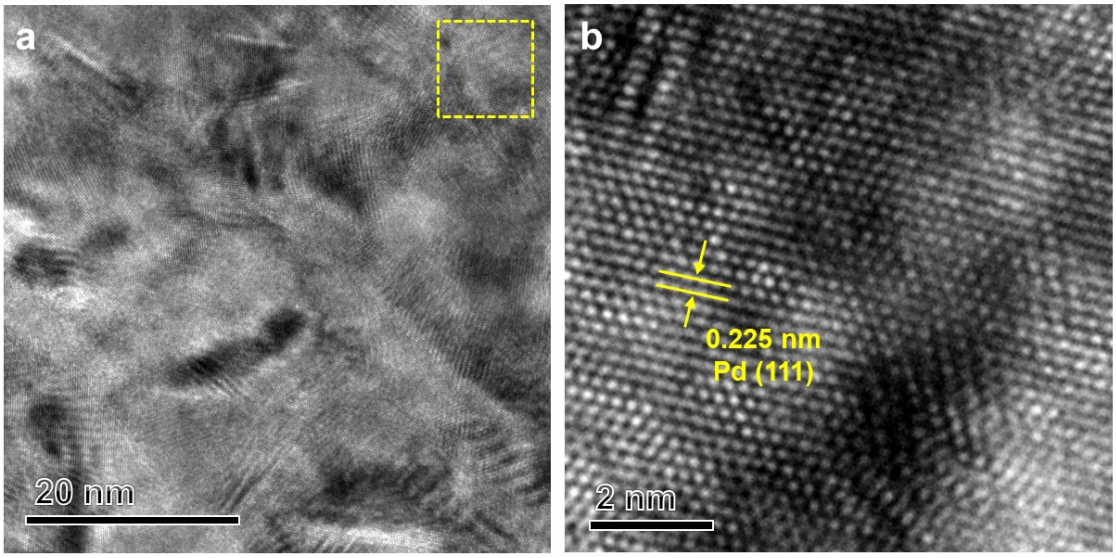


Supplementary Fig. 11 (a) High magnification TEM, and (b) HRTEM of As-Pd.

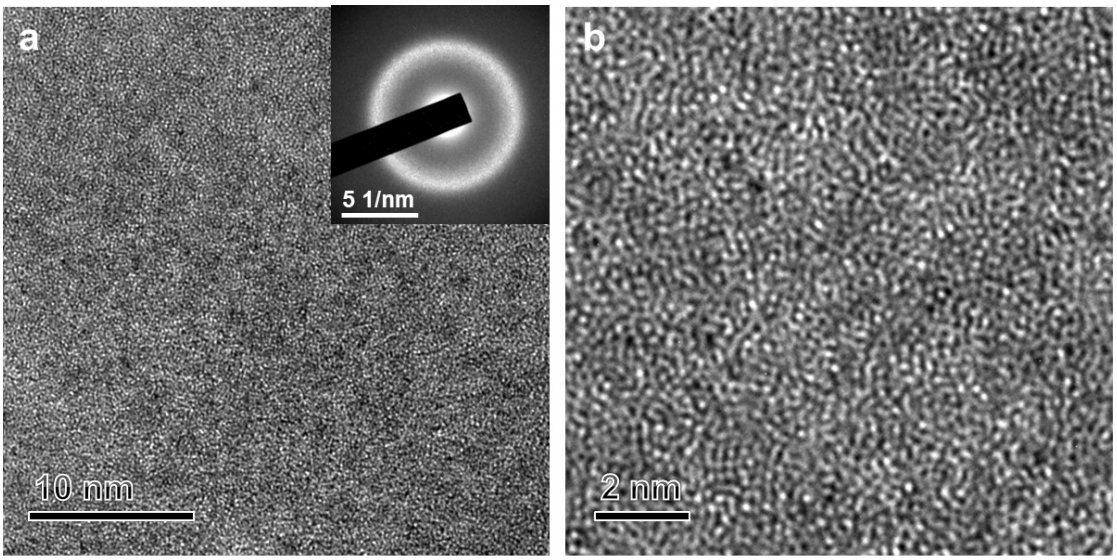


Supplementary Fig. 12 (a) High-magnification TEM, with the inset showing the corresponding SAED pattern, and (b) HRTEM of As-HEAA.

Supplementary Table 1 Elemental compositions of SNDP-Pd@HEAA samples with different O contents obtained by SEM-EDS

| $O_2$ flow rate | Pd (at%) | Al (at%) | Cu (at%) | Ni (at%) | Ti (at%) | Zn (at%) | Zr (at%) | Si (at%) | O (at%) |
|---|---|---|---|---|---|---|---|---|---|
| 0 sccm | 39.00 | 3.90 | 7.40 | 6.17 | 5.69 | 12.39 | 11.98 | 5.75 | 7.72 |
| 0.15 sccm | 36.98 | 3.72 | 7.49 | 5.87 | 5.19 | 11.24 | 10.86 | 5.40 | 13.25 |
| 0.3 sccm | 34.18 | 3.29 | 6.65 | 5.48 | 5.97 | 10.12 | 10.15 | 5.41 | 18.75 |
| 0.5 sccm | 33.88 | 3.78 | 5.88 | 4.48 | 4.07 | 8.63 | 4.82 | 5.15 | 29.31 |
| 0.75 sccm | 27.65 | 2.81 | 5.10 | 4.59 | 3.75 | 9.60 | 7.34 | 3.74 | 35.43 |
| 1 sccm | 24.52 | 2.74 | 4.62 | 3.99 | 2.90 | 8.82 | 6.41 | 3.75 | 42.24 |
| 2 sccm | 23.99 | 2.02 | 3.75 | 3.25 | 2.43 | 5.14 | 8.32 | 3.39 | 47.71 |
| 3.5 sccm | 23.51 | 1.22 | 2.38 | 2.15 | 1.01 | 1.17 | 9.73 | 2.03 | 56.80 |

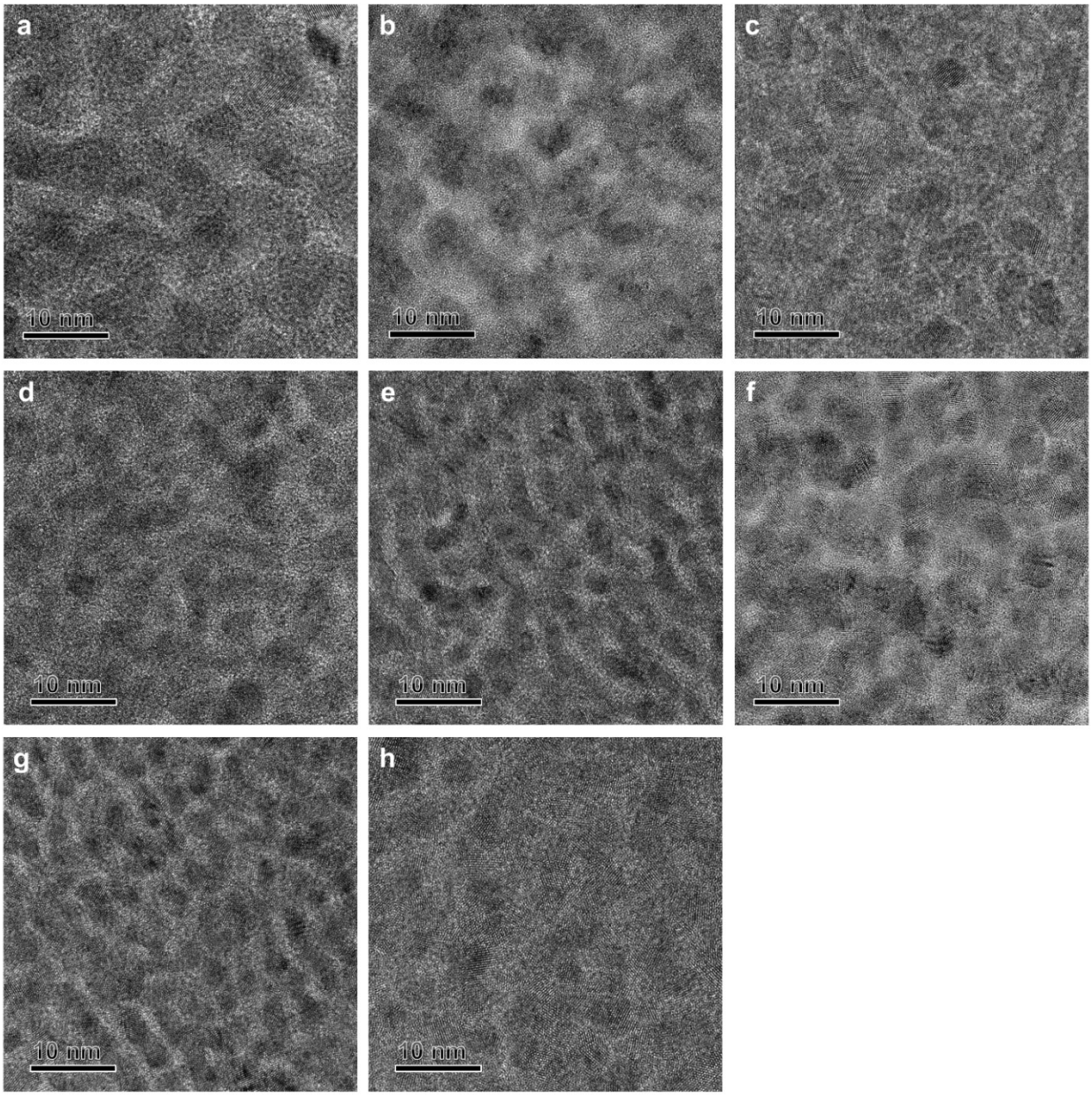


Supplementary Fig. 13 TEM of SNDP-Pd@HEAA with different O contents: (a) 7.72 at%, (b) 13.25 at%, (c) 18.75 at%, (d) 29.31 at%, (e) 35.43 at%, (f) 42.24 at%, (g) 47.71 at%, and (h) 56.80 at%.

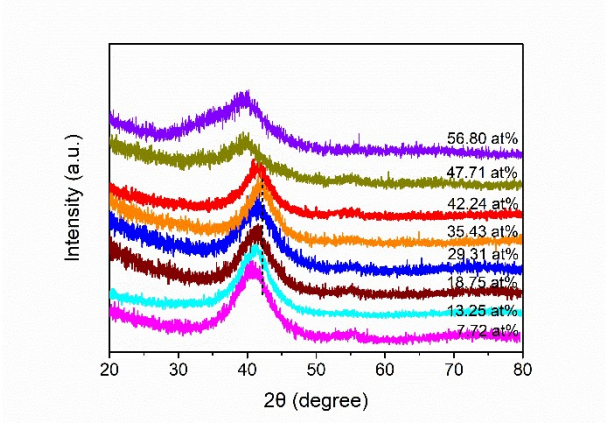


Supplementary Fig. 14 XRD patterns of SNDP-Pd@HEAA with different O contents.

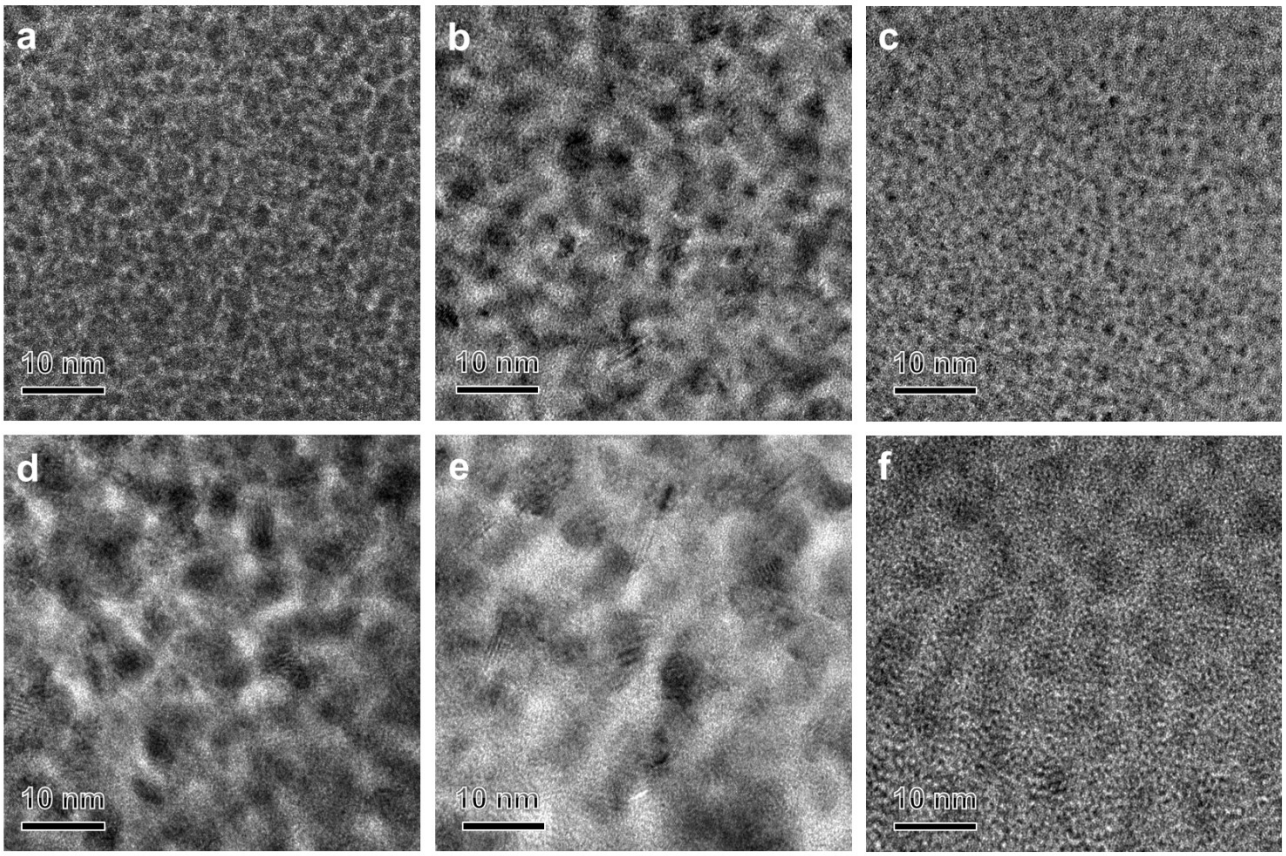


Supplementary Fig. 15 TEM of SNDP-TM@HEAA samples: (a) Ir, (b) Pt, (c) Ru, (d) Au, (e) Ag, and (f) W.

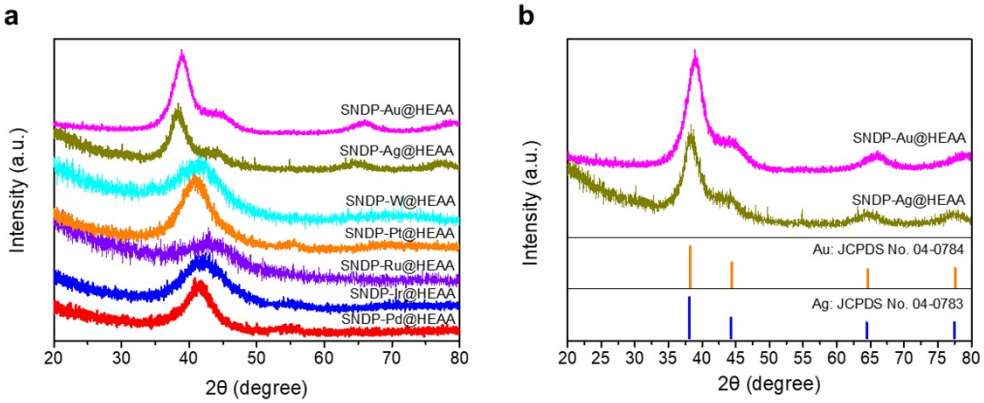


Supplementary Fig. 16 (a) XRD patterns of SNDP-TM@HEAA samples (TM = Au, Ag, W, Pt, Ru, Ir, Pd), (b) comparison of XRD patterns of SNDP-Au@HEAA and SNDP-Ag@HEAA with standard metal Au and Ag.

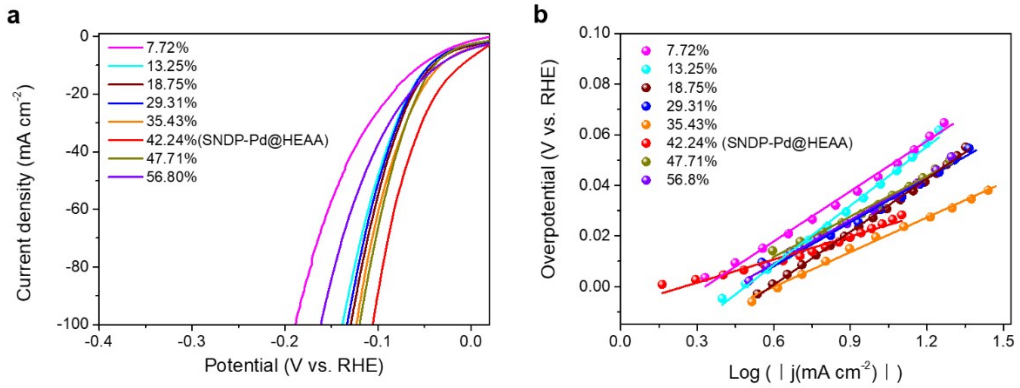


Supplementary Fig. 17 (a) Polarisation curves of the SNDP-Pd@HEAA samples with different O contents in 1 M KOH with iR correction. (b) Corresponding Tafel plots.

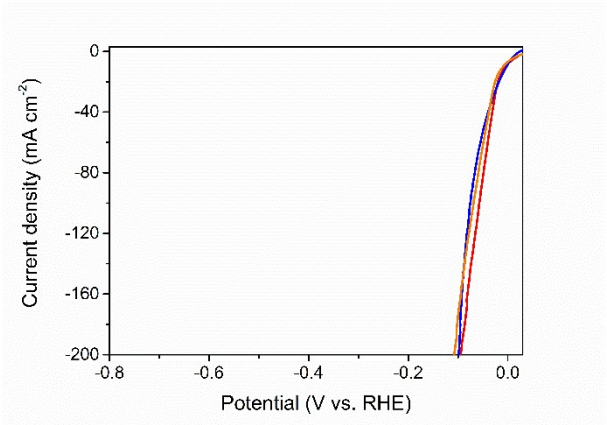


Supplementary Fig. 18 Polarisation curves of three independent SNDP-Pd@HEAA samples prepared from different batches in 1 M KOH with iR correction.

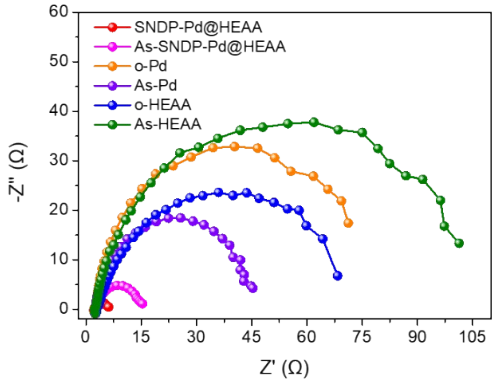


Supplementary Fig. 19 Electrochemical impedance spectroscopy of SNDP-Pd@HEAA, As-SNDP-Pd@HEAA, o-Pd, As-Pd, o-HEAA, As-HEAA, and 20% Pt/C at an overpotential of 100 mV in 1 M KOH solution at room temperature.

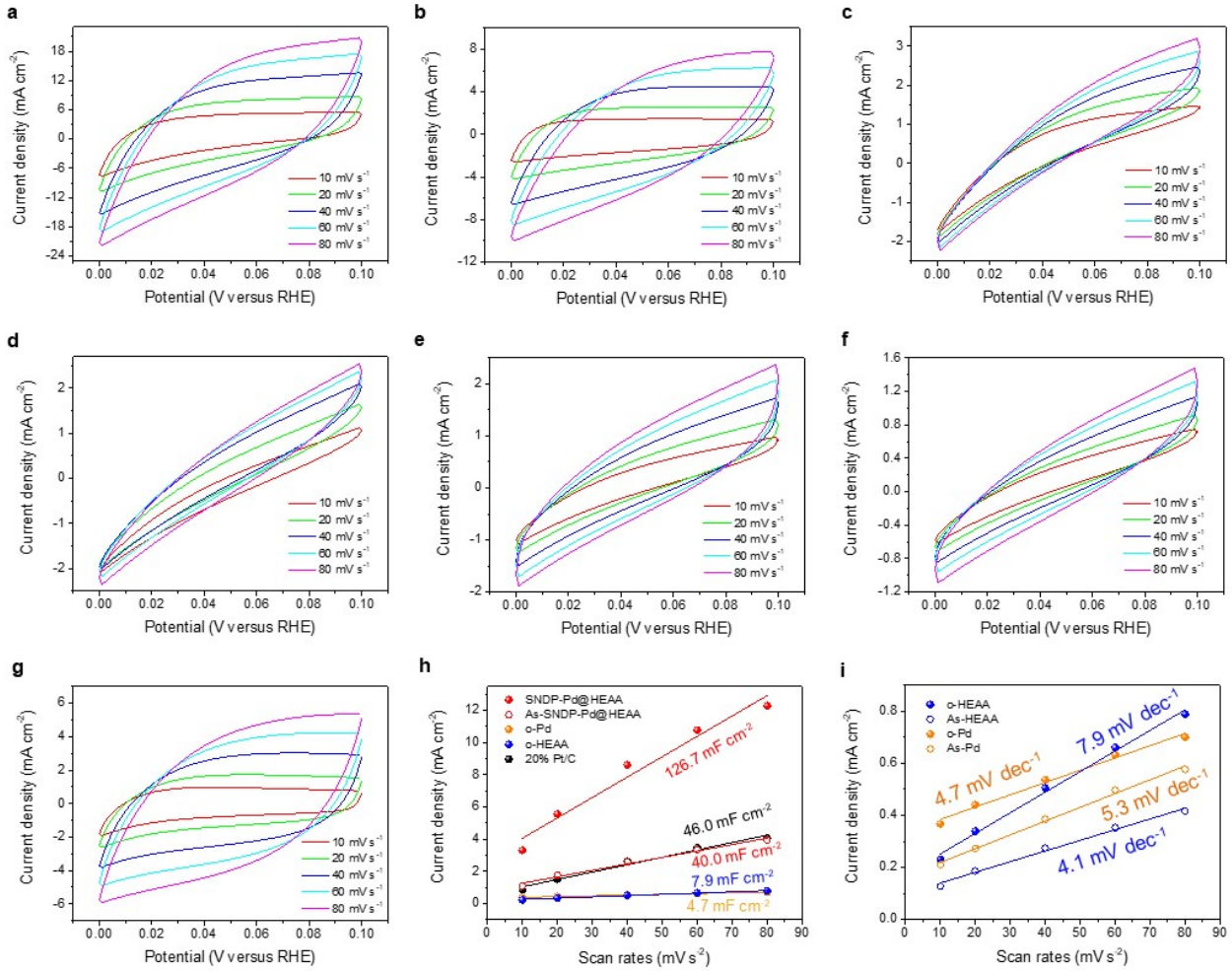


Supplementary Fig. 20 Cyclic voltammograms in the region of 0–0.1 V vs. RHE at various scan rates for (a) SNDP-Pd@HEAA, (b) As-SNDP-Pd@HEAA, (c) o-Pd, (d) As-Pd, (e) o-HEAA, (f) As-HEAA, and (g) 20% Pt/C. (h)-(i) Calculated electrochemical double-layer capacitance for the as-prepared materials.

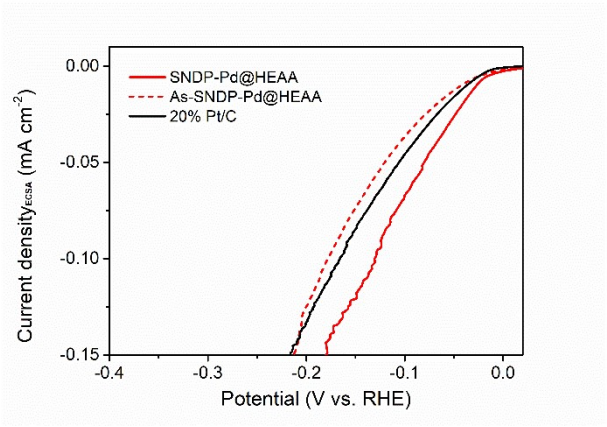


Supplementary Fig. 21 LSV curves normalized by the ECSA of SNDP-Pd@HEAA, As-SNDP-Pd@HEAA, and 20% Pt/C in an alkaline solution.

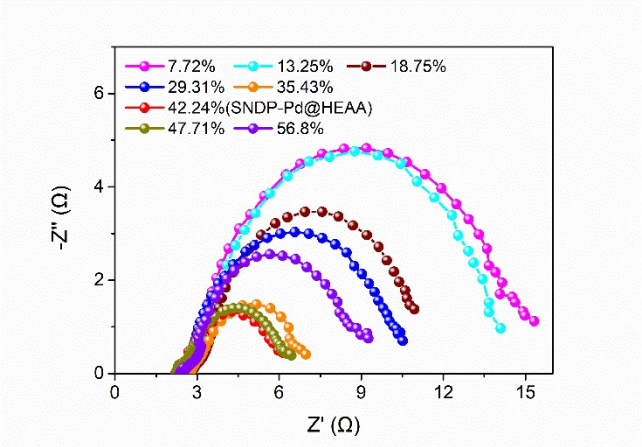


Supplementary Fig. 22 Electrochemical impedance spectroscopy of SNDP-Pd@HEAA samples with different O contents in 1 M KOH solution at an overpotential of 100 mV and room temperature.

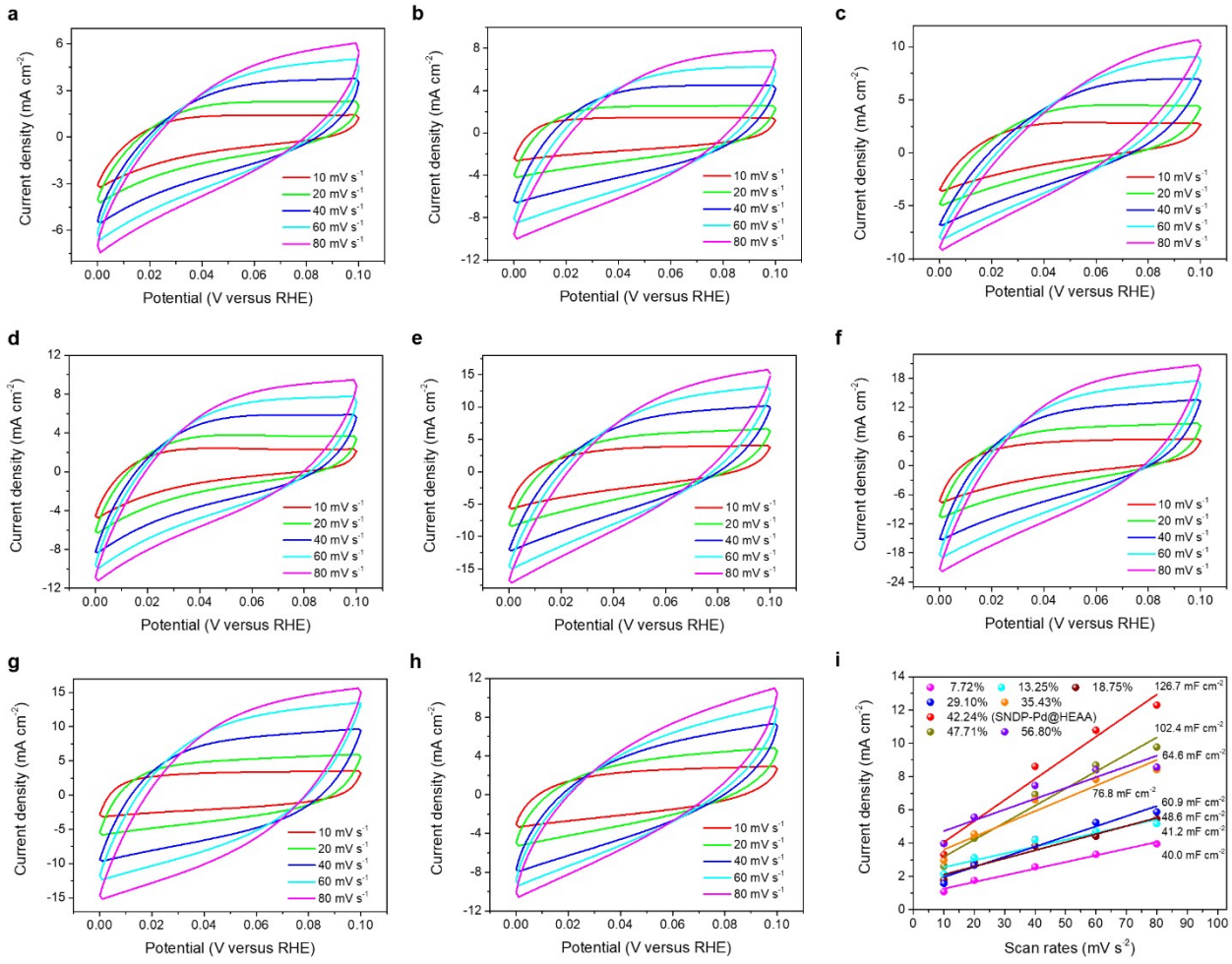


Supplementary Fig. 23 Cyclic voltammograms in the region of 0–0.1 V vs. RHE at various scan rates for SNDP-Pd@HEAA samples with different oxygen atomic contents: (a) 7.72%, (b) 13.25 at%, (c) 18.75 at%, (d) 29.31 at%, (e) 35.43 at%, (f) 42.24 at%, (g) 47.71 at%, and (h) 56.80 at%. (i) Calculated electrochemical double-layer capacitance for (a)–(g).

Supplementary Table 2 Comparison of the hydrogen evolution reaction performance of SNDP-Pd@HEAA in 1 M KOH and previously reported electrocatalysts

| **Electrocatalysts** | **Overpotential (at 10 mA cm$^{-2}$)** | **Tafel slope (mV dec$^{-1}$)** | **Ref.** |
|---|---|---|---|
| **Cystal–amorphous dual-phase catalyst** | | | |
| **SNDP-Pd@HEAA** | 10.16 | 38.9 | **This work** |
| As-SNDP-Pd@HEAA | 53.3 | 53.3 | This work |
| AlMnRu | 23.7 | / | [6] |
| Pt-a/c-CoNiHPi | 19 | 49.2 | [7] |
| CoP/$MnO_x$ | 135 | 59.4 | [8] |
| **Noble-metal-based catalyst** | | | |
| Pd-$CN_x$ | 55 | 35 | [9] |
| $Pt_3Ni_3$ NWs/C-air | 40 | / | [10] |
| 4H/fcc Au-Ru-2 NWs | 50 | 30.8 | [11] |
| 4H/fcc Ru Nanotubes | 23 | 29.4 | [12] |
| RuCo NSs | 26 | 26.3 | [13] |
| h-$RuSe_2$ | 34 | 95 | [14] |
| Ni/np-Ir | 20 | 26 | [15] |
| Ru/OMSNNC | 13 | 40.41 | [16] |
| Turing PtNiNb | 18 | 29.9 | [17] |
| **Crystal catalyst** | | | |
| Pt-Ni ASs | 27.7 | 27 | [18] |
| Co/$Co_3O_4$ nanosheets | 90 | 44 | [19] |
| $V_8C_7$@GC NSs/NF | 47 | 44 | [20] |
| $(Ni_{0.048}Fe_{0.952})_2P$ | 90 | 82.7 | [21] |
| PHA-$Mo_2C$ | 93 | 47.3 | [22] |
| PS-MoNi@NF | 72 | 37 | [23] |
| CoNiP/CoxP | 36 | 70 | [24] |
| $Mo_2C$@BNC | 99 | 58.1 | [25] |
| **Amorphous catalyst** | | | |
| Am $FePO_4$/NF | 123 | 104.49 | [26] |
| $NiWO_4/Ni_3S_2$ | 136 | 112 | [27] |
| Ni-FeP/TiN/CC | 75 | 64 | [28] |
| CoFeO@BP | 88 | 51 | [29] |
| Ni-S-Se/NF | 98 | 99.4 | [30] |
| np-$Co_{65}Mo_{15}P_{20}$ | 40.8 | 46.2 | [31] |
| **Single atom catalyst** | | | |
| $Mo_1N_1C_2$ | 132 | 90 | [32] |
| Pt/NiO@Ni/NF | 34 | 39 | [33] |

| | | | |
|---|---|---|---|
| W-SAC | 85 | 53 | [34] |
| Co1/PCN | 89 | 52 | [35] |
| E-Co SAs | 59 | 105 | [36] |
| $Fe_1$/NC | 111.1 | 86.1 | [37] |
| $Pt_1$/N-C | 46 | 36.8 | [38] |
| $Pt_{SA}$-NiO/Ni | 26 | 27.07 | [39] |
| Ru-$MoS_2$/CC | 41 | 114 | [40] |
| RuAu-0.2 SAA | 24 | 37 | [41] |
| **Hybrid catalyst** | | | |
| NiO/Ni-CNT | 100 | 81 | [42] |
| CuCoO-NWs | 140 | 108 | [43] |
| $Ni(OH)_2/MoS_2$ | 80 | 60 | [44] |
| $Cu_3P–Ni_2P$/NF | 103 | 80 | [45] |
| 1% Pd-$CeO_{2-x}$-NC | 115 | 58 | [46] |
| Pt/Nb-$Co(OH)_2$ | 112 | 82 | [47] |
| $Ru_{NP}$-$Ru_{SA}$@CFN-800 | 33 | 37.16 | [48] |
| Pt/Co-N-C | 33 | 36.8 | [49] |
| **Multicomponent alloys (at least four elements)** | | | |
| PtAuPdRhRu/carbon-700 | ~120 | 62 | [50] |
| CuAlNiMoFe | 56@100 mA $cm^{-2}$ | 60 | [51] |
| FeCoNiAlTi | 88.2 | 40.1 | [52] |
| Nanosponge PdPtCuNiP | 32 | 37.4 | [53] |
| FeCoNiCuPd/CFC | 29.7 | 47.2 | [54] |
| $Pt_{25}Pd_{25}Ni_{25}P_{25}$ | 19.8 | 40 | [55] |
| $(FeCoNiB_{0.75})_{97}Pt_3$ | 27 | | [56] |
| $Pt_4$FeCoCuNi | 20 | 31 | [57] |

**Obtained from figures in the reference.*

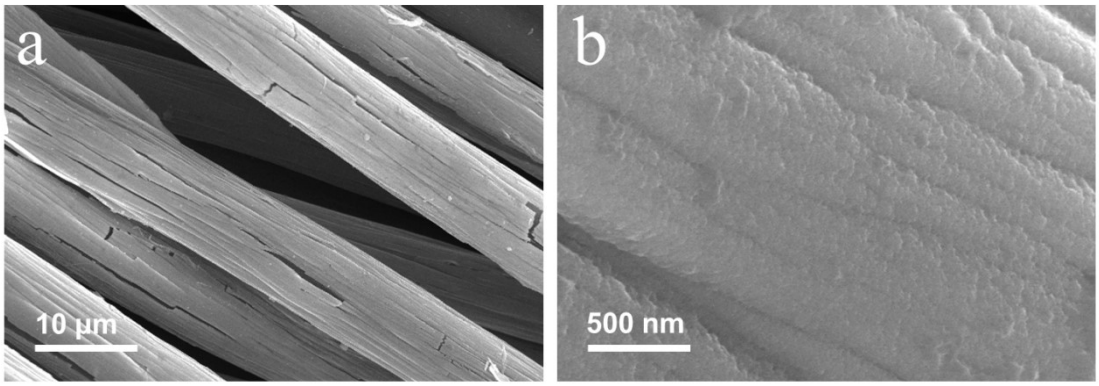


Supplementary Fig. 24 SEM images of SNDP-Pd@HEAA on carbon cloth after 100 h in 1M KOH (stability test).

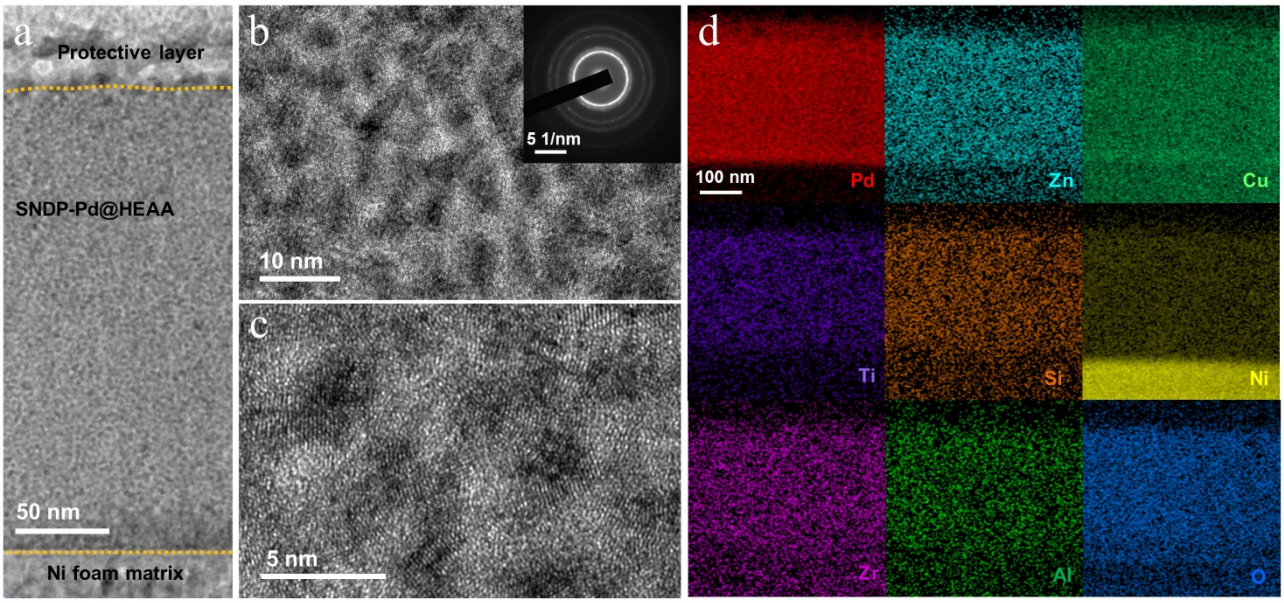


Supplementary Fig. 25 (a) Low-magnification TEM image, (b) high-magnification TEM image, where the inset shows the corresponding SEAD pattern, (c) HRTEM image, and (d) EDS elemental mapping of Pd (red), Zn (cyan), Cu (light green), Ti (purple), Si (orange), Ni (yellow), Zr (violet), Al (green), and O (blue) for SNDP-Pd@HEAA after 100 h in 1M KOH.

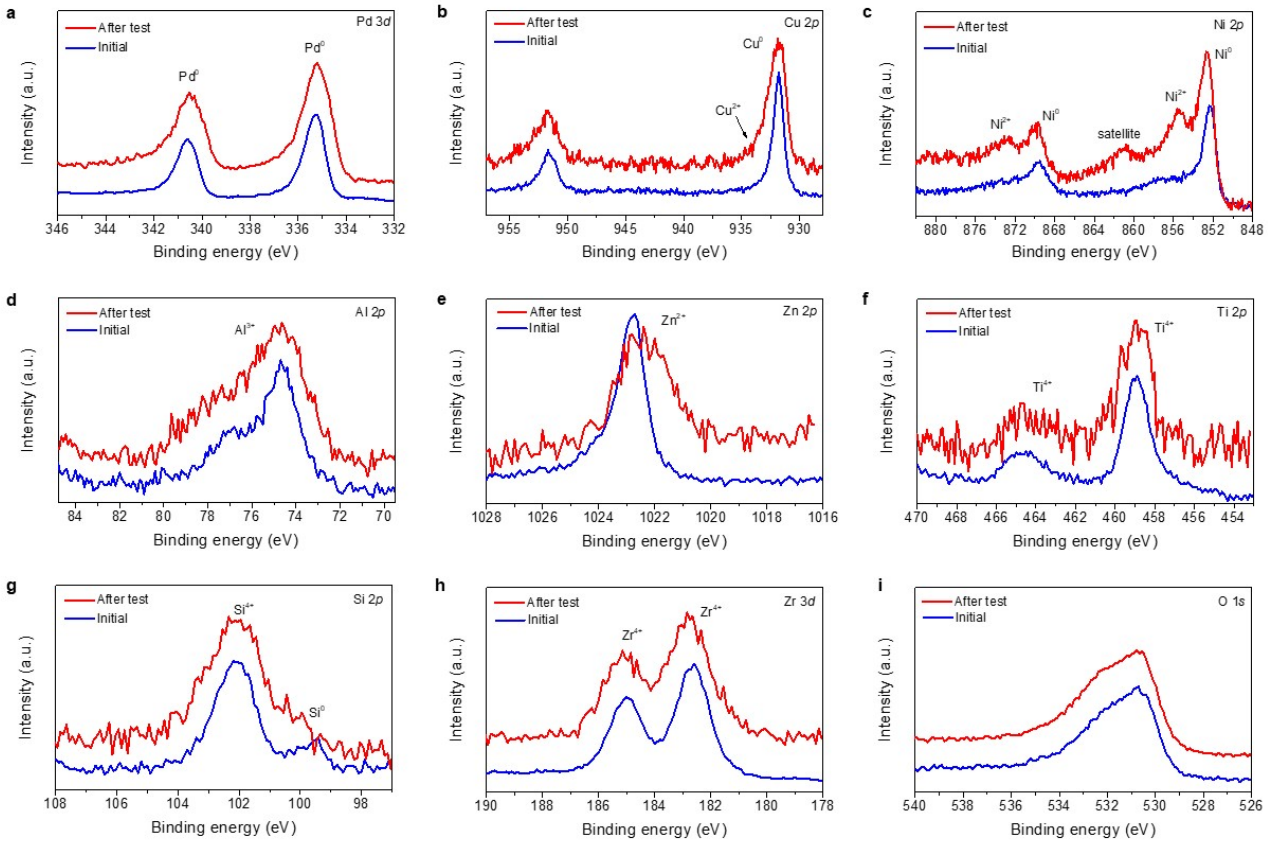


Supplementary Fig. 26 (a) Pd 3*d*, (b) Cu 2*p*, (c) Ni 2*p*, (d) Al 2*p*, (e) Zn 2*p*, (f) Ti 2*p*, (g) Si 2*p*, (h) Zr 3*d*, and (i) O 1*s* X-ray photoelectron microscopy of SNDP-Pd@HEAA after 100 h in 1M KOH.

Supplementary Table 3 Elemental compositions determined by SEM-EDS for SNDP-Pd@HEAA before and after stability test.

| | Pd (at%) | Al (at%) | Cu (at%) | Ni (at%) | Ti (at%) | Zn (at%) | Zr (at%) | Si (at%) | O (at%) |
|---|---|---|---|---|---|---|---|---|---|
| Before test | 24.52 | 2.74 | 4.62 | 3.99 | 2.90 | 8.82 | 6.41 | 3.75 | 42.24 |
| After test | 23.81 | 2.51 | 4.83 | 3.97 | 2.75 | 8.44 | 6.16 | 3.38 | 44.15 |

Supplementary Table 4 Elemental compositions determined by XPS for SNDP-Pd@HEAA before and after stability test.

| | Pd (at%) | Al (at%) | Cu (at%) | Ni (at%) | Ti (at%) | Zn (at%) | Zr (at%) | Si (at%) | O (at%) |
|---|---|---|---|---|---|---|---|---|---|
| Before test | 21.1 | 4.0 | 4.4 | 4.6 | 2.8 | 6.4 | 4.9 | 3.7 | 48.1 |
| After test | 20.2 | 3.5 | 4.5 | 4.3 | 2.6 | 5.9 | 4.9 | 3.3 | 50.71 |

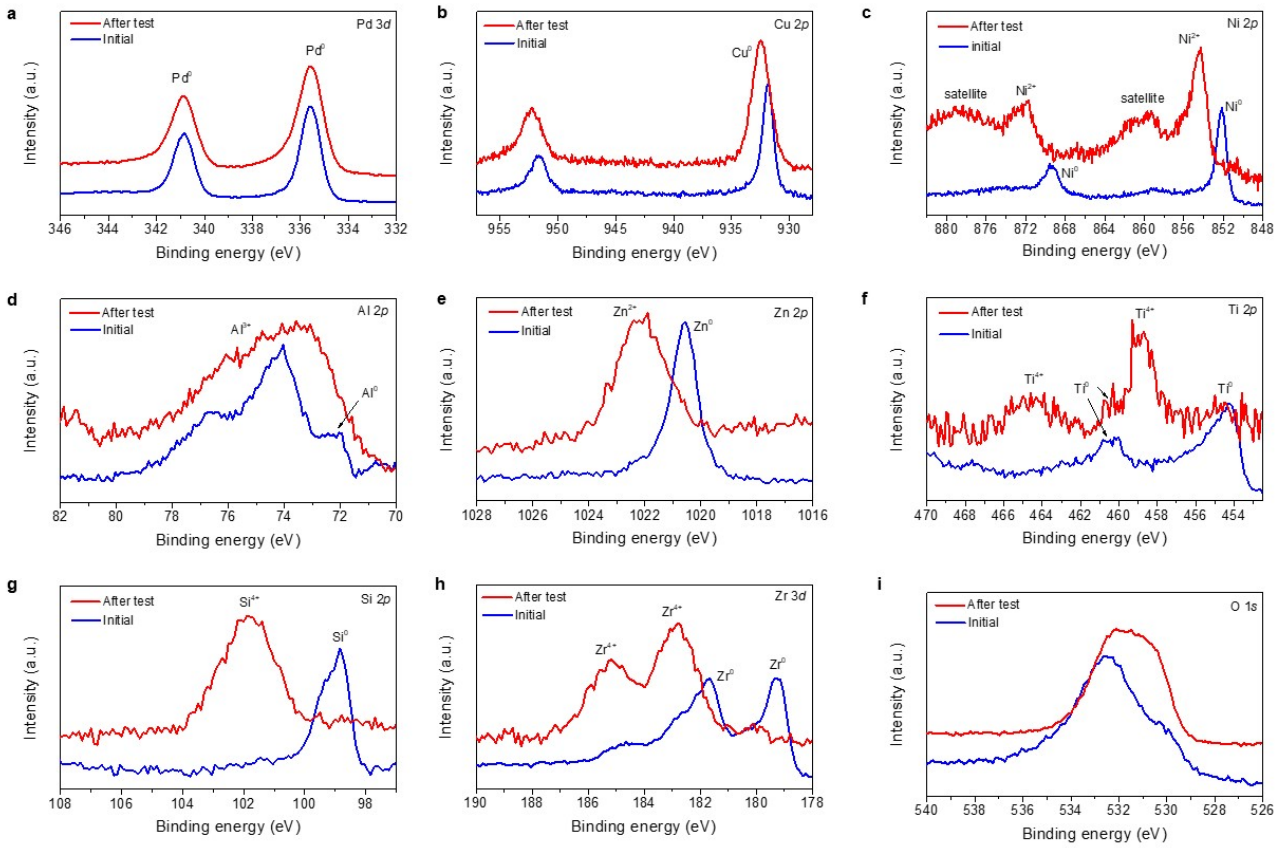


Supplementary Fig. 27 (a) Pd 3*d*, (b) Cu 2*p*, (c) Ni 2*p*, (d) Al 2*p*, (e) Zn 2*p*, (f) Ti 2*p*, (g) Si2*p*, (h) Zr 3*d*, and (i) O 1*s* X-ray photoelectron microscopy of As-SNDP-Pd@HEAA after 100 h in 1 M KOH.

Supplementary Table 5 ICP-OES results for SNDP-Pd@HEAA after 200 h at current density of 200 mA $cm^{-2}$

| | Concentration (mmol/L) | Limit of reporting (mmol/L) |
|---|---|---|
| Pd | 0.0020 | 0.00041 |
| Al | 0.0026 | 0.00104 |
| Zn | 0.0017 | 0.00009 |
| Ti | 0.0012 | 0.00008 |
| Zr | 0.0005 | 0.000078 |
| Si | 0.4321 | 0.0020 |
| Cu | 0.0023 | 0.00015 |
| Ni | 0.0039 | 0.00026 |
| O | / | / |

**The lowest concentration of a substance that can be reliably measured by ICP-OES.*

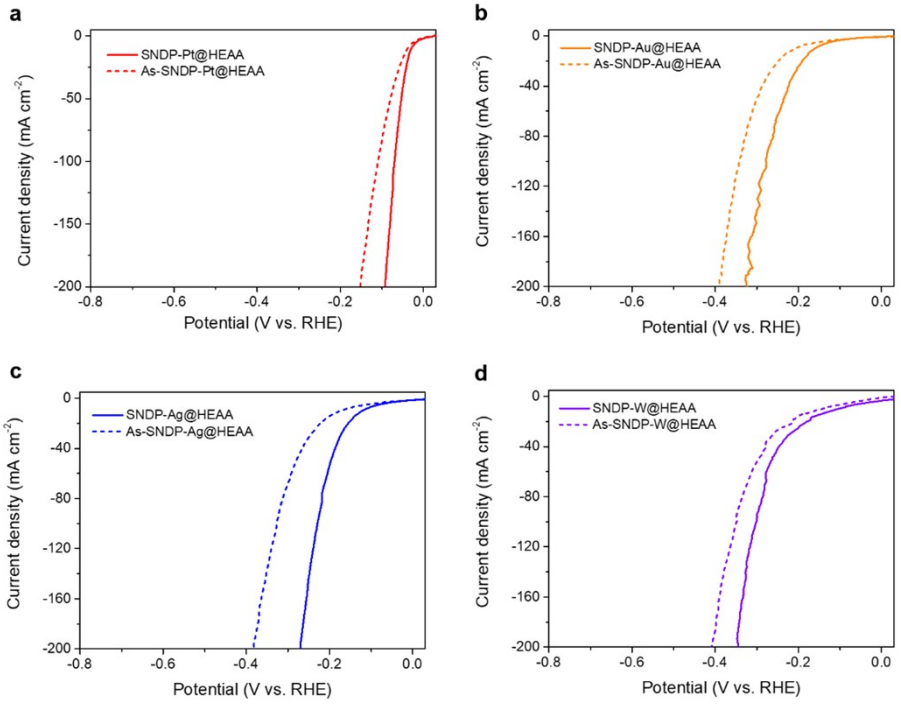


Supplementary Fig. 28 Polarisation curves of (a) SNDP-Pt@HEAA and As-SNDP-Pt@HEAA, (b) SNDP-Au@HEAA and As-SNDP-Au@HEAA, (c) SNDP-Ag@HEAA and As-SNDP-Ag@HEAA, and (d) SNDP-W@HEAA and As-SNDP-W@HEAA in 1 M KOH with iR correction.

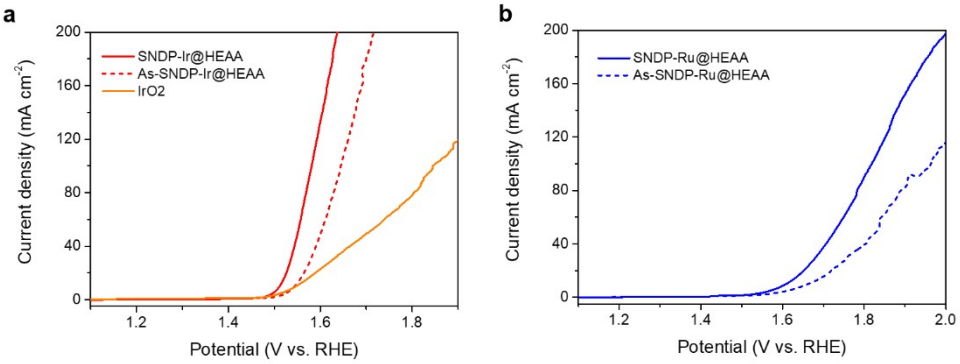


Supplementary Fig. 29 Polarisation curves of (a) SNDP-Ir@HEAA, As-SNDP-Ir@HEAA, and $IrO_2$ and (b) SNDP-Ru@HEAA and As-SNDP-Ru@HEAA in 1 M KOH with iR correction.

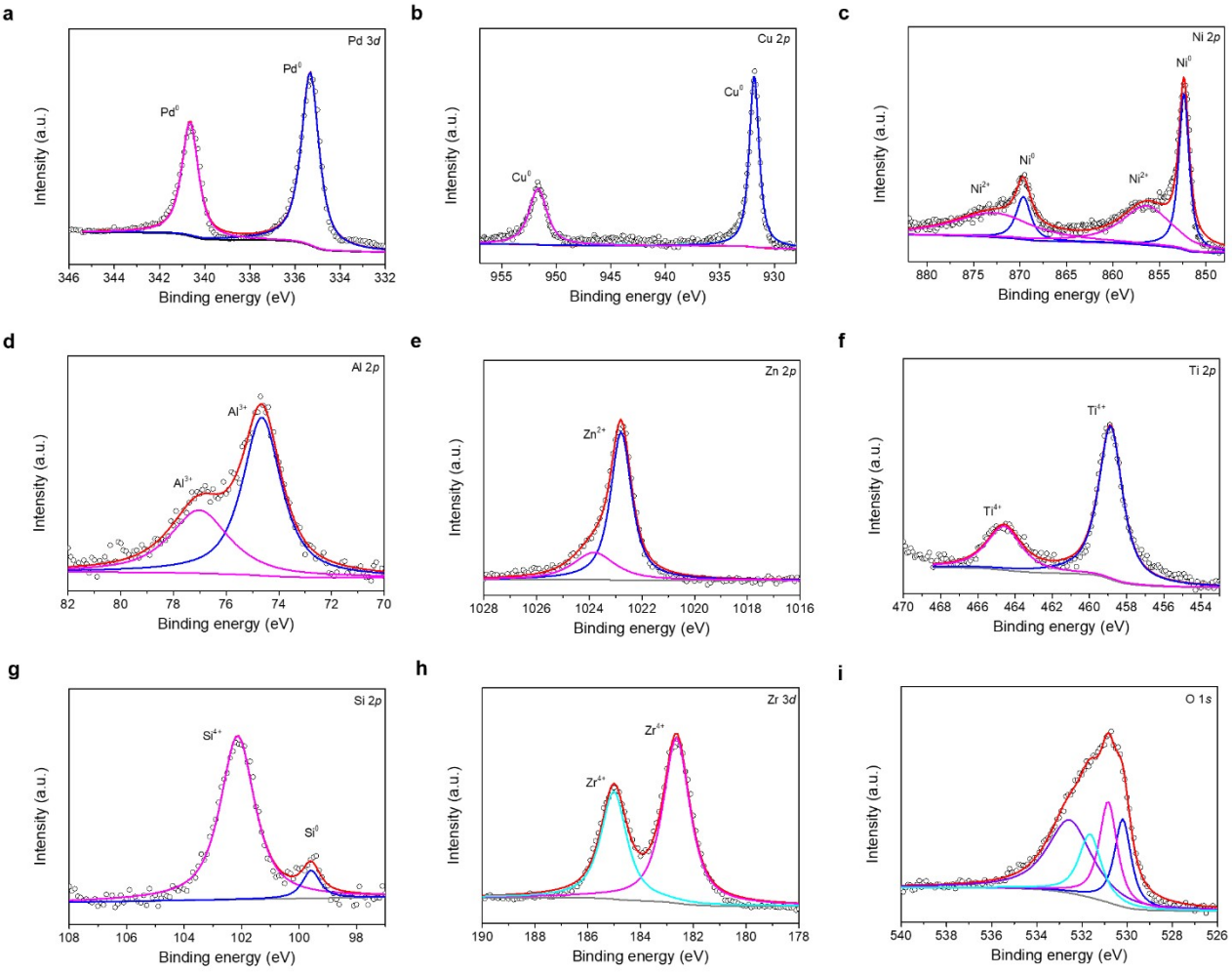


Supplementary Fig. 30 (a) Pd 3*d*, (b) Cu 2*p*, (c) Ni 2*p*, (d) Al 2*p*, (e) Zn 2*p*, (f) Ti 2*p*, (g) Si 2*p*, (h) Zr 3*d*, and (i) O 1*s* X-ray photoelectron microscopy of SNDP-Pd@HEAA with detailed fitting peaks.

Supplementary Table 6 Extended X-ray absorption fine structure (EXAFS) fitting parameters at the Pd K-edge for SNDP-Pd@HEAA and o-Pd ($S_0^2$ = 0.82)

| | Shell | *CN* | *R* (Å) | $\sigma^2$ | $\Delta E_0$ | *R* factor |
|---|---|---|---|---|---|---|
| Pd foil | Pd-Pd | 12 | 2.74 ± 0.01 | 0.0055 | 7.1 ± 0.4 | 0.0041 |
| PdO | Pd-O | 3.8 ± 0.2 | 2.03 ± 0.01 | 0.0020 | 2.8 ± 1.1 | 0.0038 |
| | Pd-Pd | 4.6 ± 0.3 | 3.06 ± 0.01 | 0.0033 | | |
| | Pd-Pd1 | 4.5 ± 0.4 | 3.46 ± 0.01 | 0.0020 | | |
| SNDP-Pd@HEAA | Pd-O | 0.3 ± 0.2 | 2.02 ± 0.06 | 0.0014 | 0.8 ± 1.1 | 0.0106 |
| | Pd-M | 1.0 ± 0.2 | 2.58 ± 0.01 | 0.0016 | | |
| | Pd-Pd | 7.3 ± 0.5 | 2.68 ± 0.02 | 0.0100 | | |
| o-Pd | Pd-O | 2.6 ± 0.4 | 2.00 ± 0.01 | 0.0030 | 3.6 ± 1.5 | 0.0078 |
| | Pd-Pd | 6.2 ± 0.7 | 2.77 ± 0.02 | 0.0167 | | |
| | Pd-Pd1 | 4.9 ± 0.8 | 3.02 ± 0.01 | 0.0090 | | |
| | Pd- Pd2 | 1.3 ± 0.2 | 3.41 ± 0.01 | 0.0011 | | |

*CN*: coordination number; *R*: bond distance; $\sigma^2$: Debye–Waller factor; $\Delta E_0$: inner potential correction; *R* factor: goodness of fit; M = Cu, Ni, Zn.

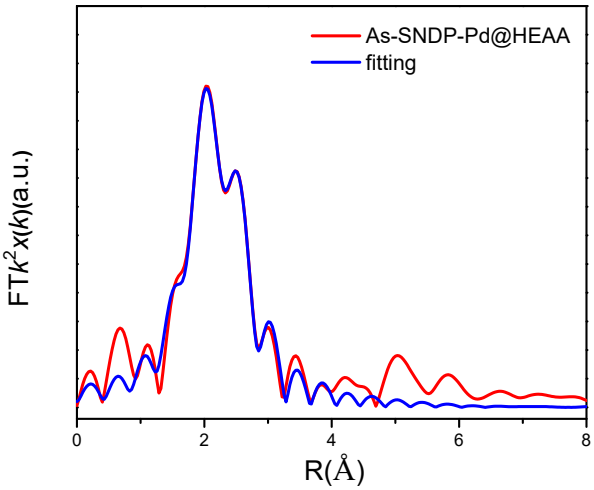


Supplementary Fig. 31 Fitting of the $k^2$-weighted Fourier transform of the extended X-ray absorption fine structure (EXAFS) spectra at the Pd K-edge of As-SNDP-Pd@HEAA.

Supplementary Table 7 EXAFS fitting parameters at the Pd K-edge for As-SNDP-Pd@HEAA ($S_0^2$ = 0.84)

| | Shell | *CN* | *R* (Å) | $\sigma^2$ | $\Delta E_0$ | *R* factor |
|---|---|---|---|---|---|---|
| Pd foil | Pd-Pd | 12 | 2.74 ± 0.01 | 0.0056 | 4.0 ± 0.3 | 0.0021 |
| PdO | Pd-O | 4.0 ± 0.2 | 2.02 ± 0.01 | 0.0020 | 6.0 ± 1.0 | 0.0075 |
| | Pd-Pd | 3.9 ± 0.3 | 3.05 ± 0.01 | 0.0033 | | |
| | Pd-Pd1 | 4.2 ± 0.3 | 3.45 ± 0.01 | 0.0020 | | |
| As-SNDP-Pd@HEAA | Pd-M | 6.7 ± 0.4 | 2.60 ± 0.01 | 0.0198 | –4.4 ± 1.3 | 0.0095 |
| | Pd-Pd | 4.0 ± 0.4 | 2.75 ± 0.01 | 0.0088 | | |
| | Pd-Zr | 0.6 ± 0.2 | 3.00 ± 0.01 | 0.0014 | | |

*CN*: coordination number; *R*: bond distance; $\sigma^2$: Debye–Waller factor; $\Delta E_0$: inner potential correction; *R* factor: goodness of fit; M = Cu, Ni, Zn.

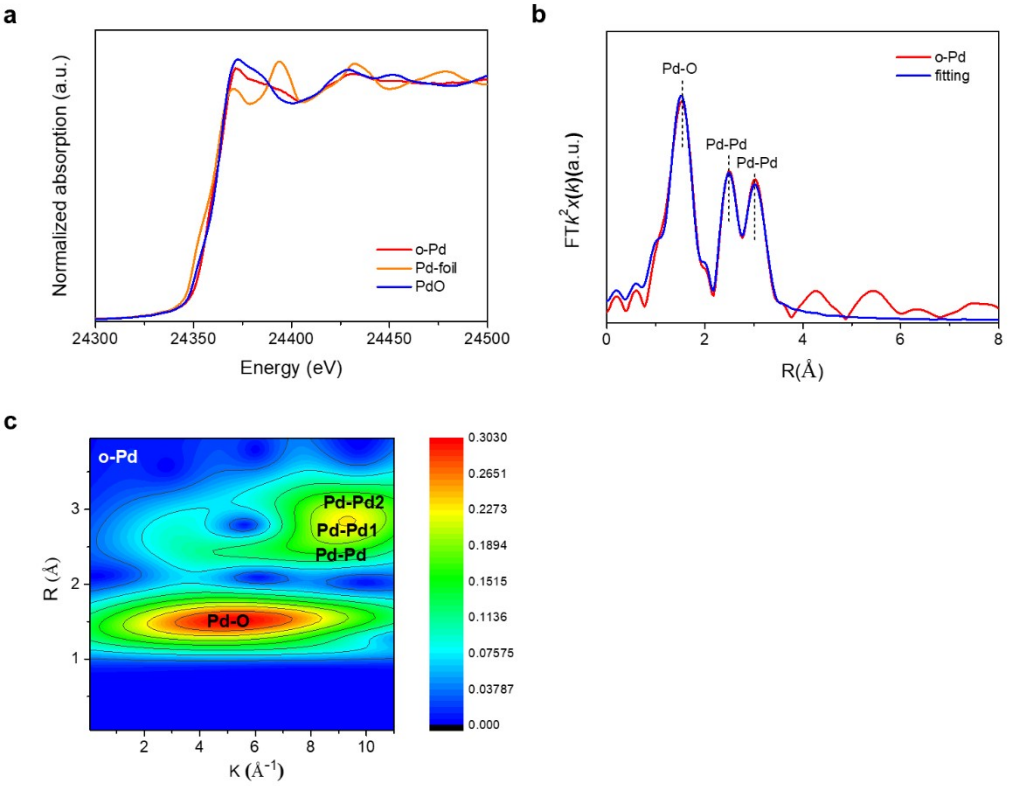


Supplementary Fig. 32 (a) X-ray absorption near edge structure spectra, (b) corresponding $k^2$-weighted Fourier transform of the EXAFS spectrum and its fitting, (c) wavelet transforms for $k^2$-weighted EXAFS signals at the Pd K-edge of o-Pd.

Supplementary Table 8 The number and percentage of different atoms in the crystal and amorphous models.

| Element | Crystal (number/at%) | Crystal-O (number/at%) | MG (number/at%) | MG-O (number/at%) |
|---|---|---|---|---|
| Al | 3/4.69 | 3/4.41 | 7/9.33 | 5/6.67 |
| Si | 6/9.38 | 6/8.82 | 16/21.33 | 10/13.33 |
| Ti | 2/3.13 | 2/2.94 | 11/14.67 | 7/9.33 |
| Ni | 5/7.81 | 5/7.35 | 5/6.67 | 3/4.00 |
| Cu | 6/9.38 | 6/8.82 | 6/8.00 | 4/5.33 |
| Zn | 4/6.25 | 4/5.88 | 3/4.00 | 2/2.67 |
| Zr | 4/6.25 | 4/5.88 | 17/22.67 | 11/14.67 |
| Pd | 34/53.13 | 34/50.00 | 10/13.33 | 6/8.00 |
| O | 0/0.00 | 4/5.88 | 0/0.00 | 27/36.00 |
| **Total** | **64/100.00** | **68/100.00** | **75/100.00** | **75/100.00** |

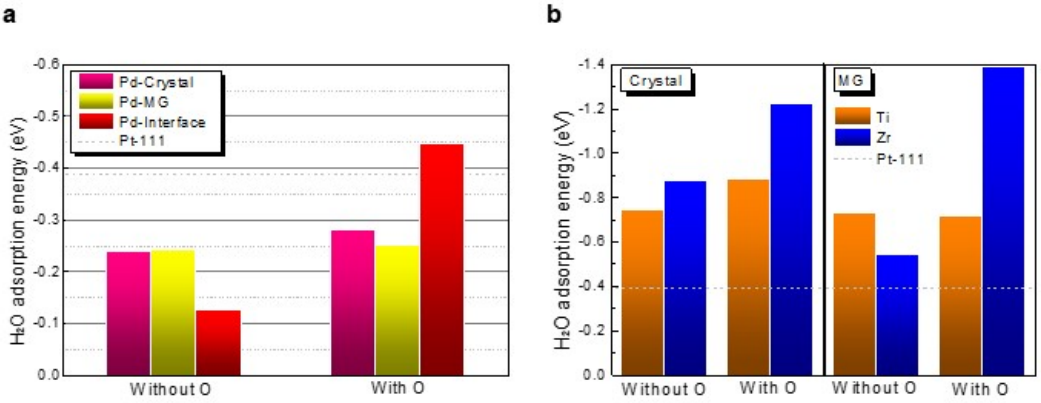


Supplementary Fig. 33 DFT calculation of $\Delta E_{H2O}$ of $H_2O$ molecules at Pd sites in crystal, amorphous, and interface models with and without elemental O. For reference, $\Delta E_{H2O}$ of the Pt(111) surface is marked by a grey dashed line.

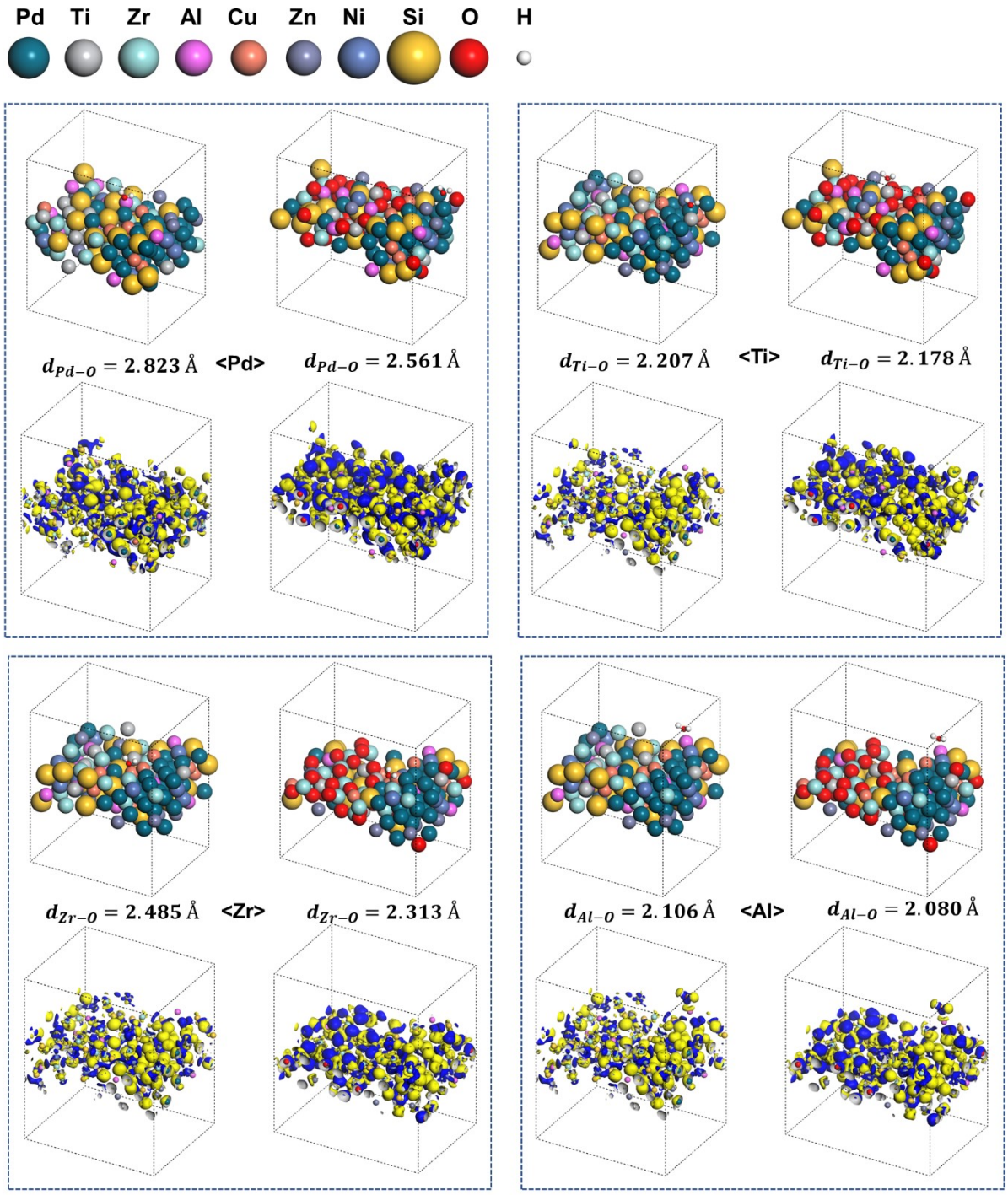


Supplementary Fig. 34 DFT simulations of atomic configurations and the corresponding electron density difference after $H_2O$ adsorption at Pd, Ti, Zr, and Al sites in the interface models with and without elemental O. The yellow and blue isosurfaces respectively represent the depletion and segregation of electrons. $d_{X\text{-}O}$ represents the bonding distances between the O atom at the $H_2O$ and Pd, Ti, Zr, and Al sites.

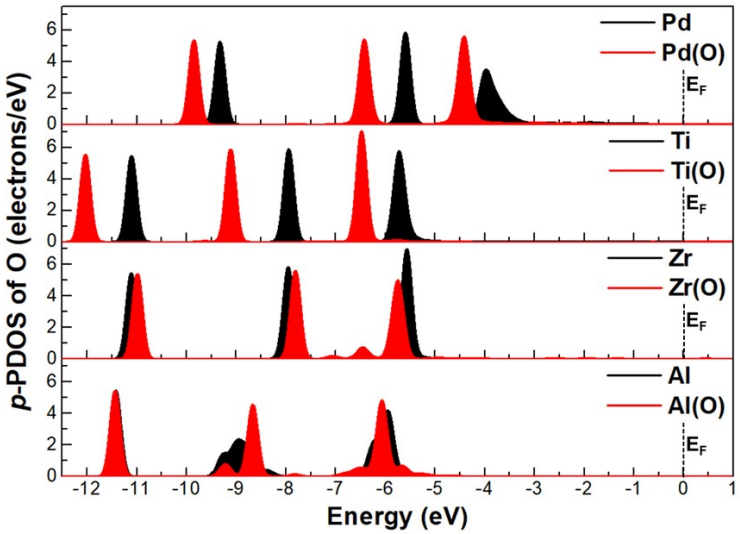


Supplementary Fig. 35 *p*-PDOS of the O atom in an $H_2O$ molecule after $H_2O$ adsorption onto Pd, Ti, Zr, and Al sites in the interface models with and without elemental O, respectively. The black dashed lines at zero energy indicate the Fermi level ($E_F$).

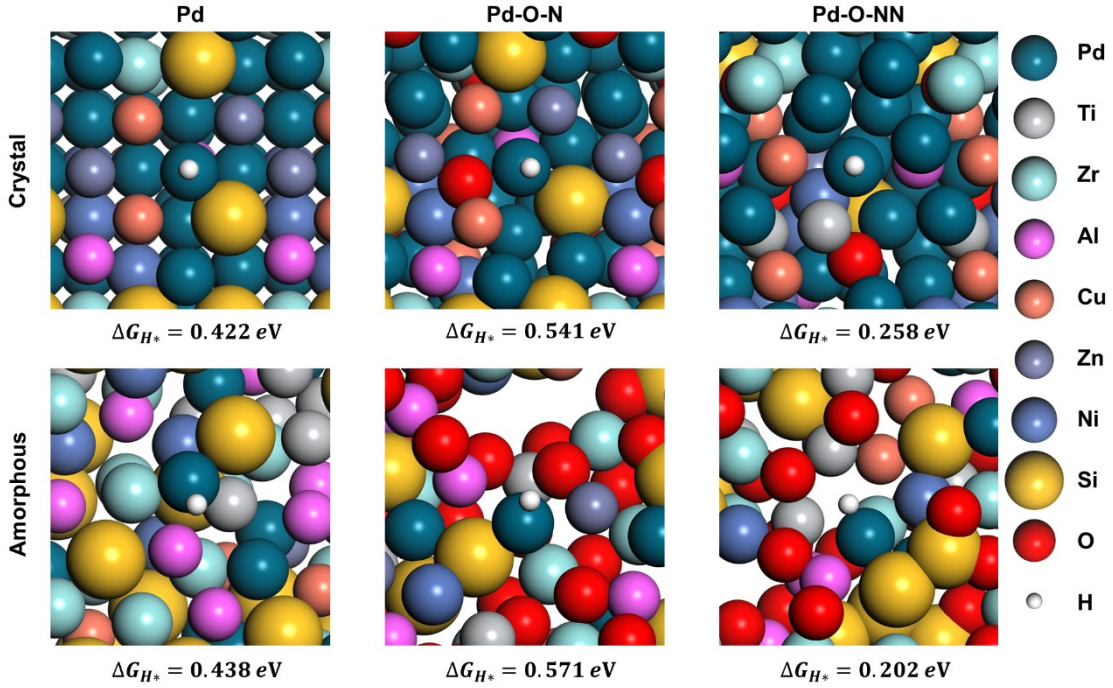


Supplementary Fig. 36 Local chemical environment after H* adsorption at Pd top sites in the crystal and amorphous models without O coordination, with nearest O coordination, and with next-nearest O coordination.

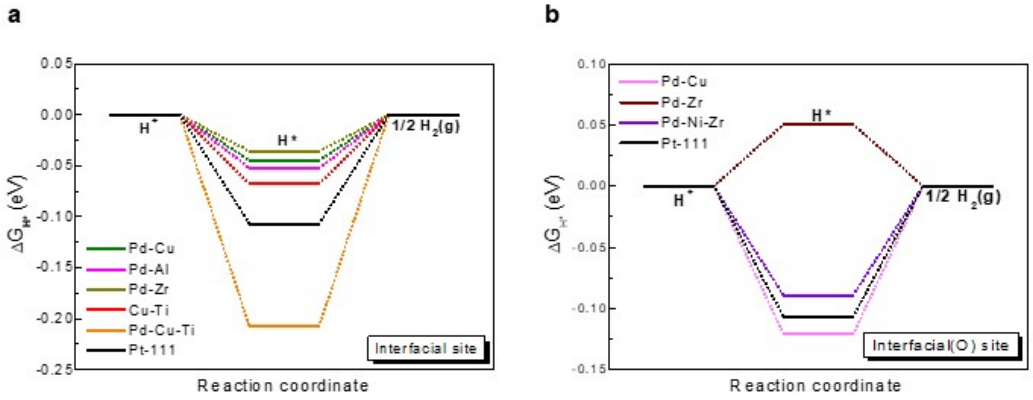


Supplementary Fig. 37 Gibbs free energy ($\Delta G_{H^*}$) profiles for various bridge and hollow sites in crystalline/amorphous interface models (a) without elemental O and (b) with elemental O.

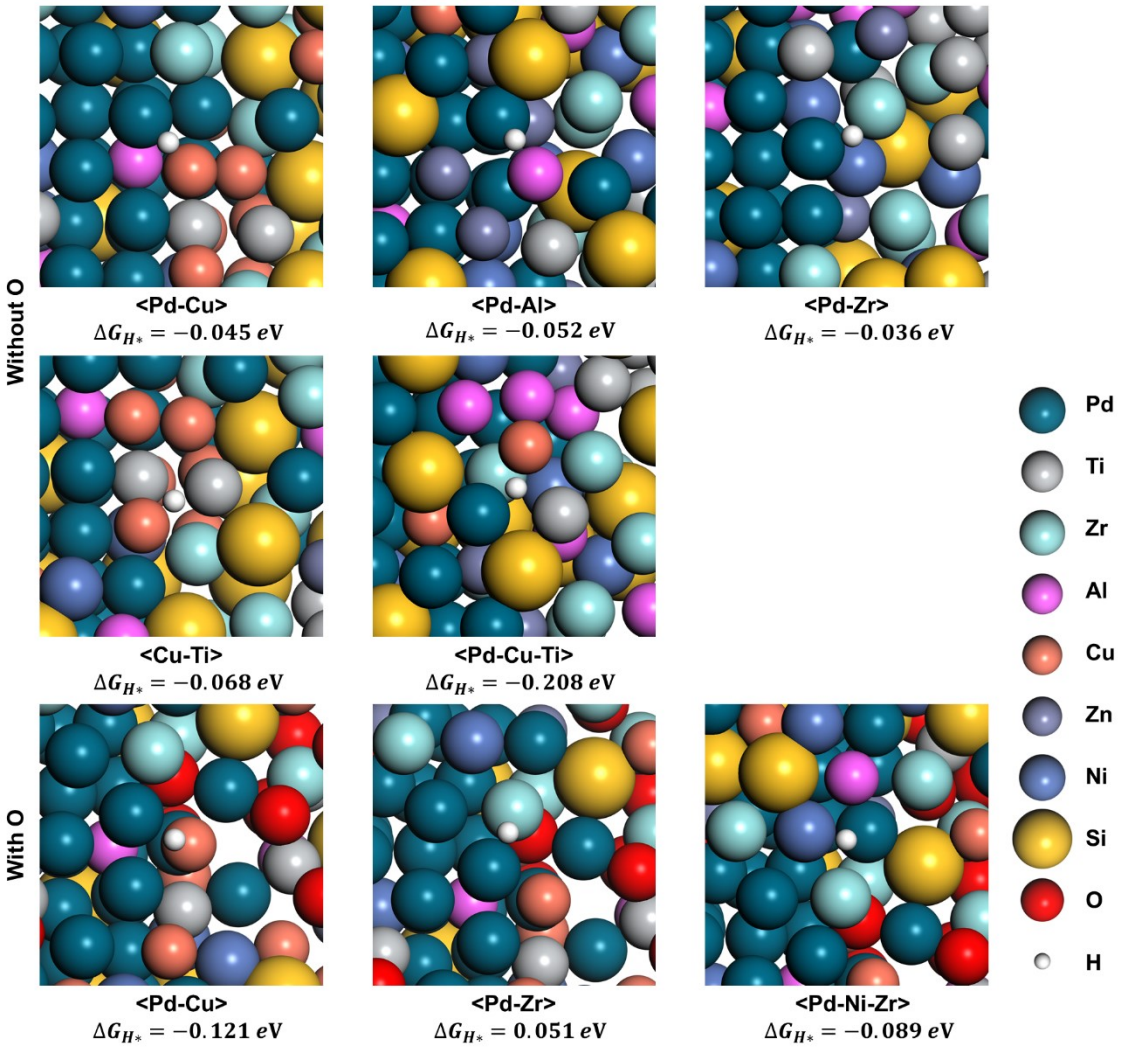


Supplementary Fig. 38 Local chemical environment of various H* adsorption sites (bridge and hollow) in crystalline/amorphous interface models without and with elemental O.

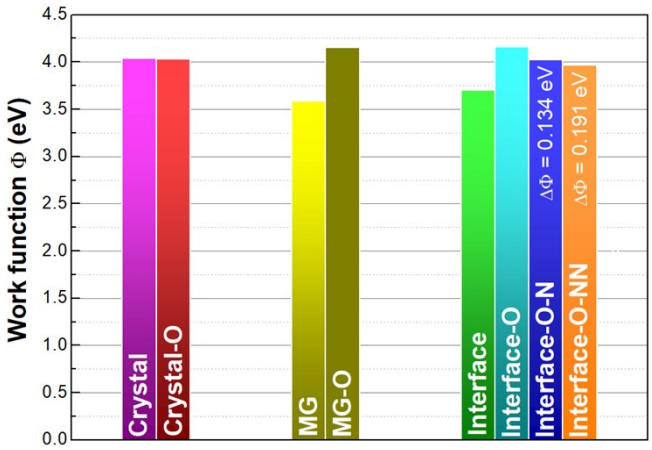


Supplementary Fig. 39 The values of work functions of various samples modeled for DFT calculations. ΔΦ is the change of change of work function after hydrogen adsorption onto the Pd sites with nearest and next-nearest O coordination.

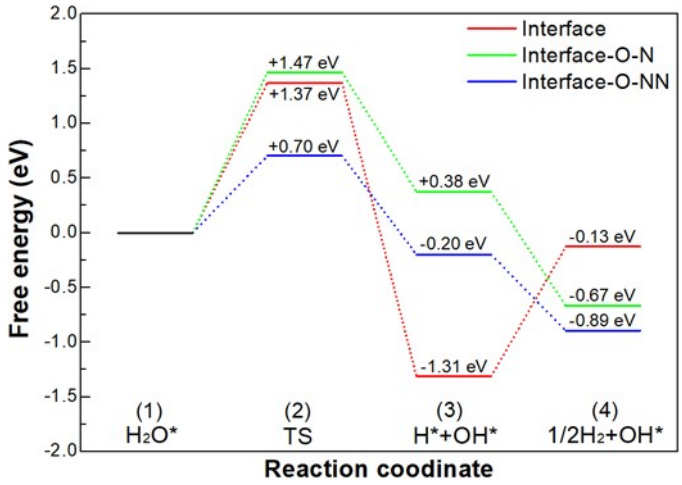


Supplementary Fig. 40 DFT calculation of HER activation energy on the interfacial catalysts. $\Delta E_{2\text{-}1}$ and $\Delta E_{4\text{-}3}$ are the related kinetic energy barriers for water dissociation and $H_2$ formation on the surface of the catalysts, respectively.

## References


1. S. J. Clark, M. D. Segall, C. J. Pickard, P. J. Hasnip, M. I. Probert, K. Refson and M. C. Payne, *Zeitschrift für kristallographie-crystalline materials*, 2005, **220**, 567-570.
2. J. P. Perdew, K. Burke and M. Ernzerhof, *Physical review letters*, 1996, **77**, 3865.
3. D. Vanderbilt, *Physical review B*, 1990, **41**, 7892.
4. H. J. Monkhorst and J. D. Pack, *Physical review B*, 1976, **13**, 5188.
5. J. K. Nørskov, T. Bligaard, A. Logadottir, J. Kitchin, J. G. Chen, S. Pandelov and U. Stimming, *Journal of The Electrochemical Society*, 2005, **152**, J23.
6. S. Liu, H. Li, J. Zhong, K. Xu, G. Wu, C. Liu, B. Zhou, Y. Yan, L. Li and W. Cha, *Science Advances*, 2022, **8**, eadd6421.
7. Y. Li, X. Zhang, L. Liu, H. Sheng, C. Li, L. Cao, H. Li, C. Xia and B. Dong, *Small*, 2023, 2300368.
8. M. Jin, M. Teng, S. Wang, K. Yang, J. Wang and H. Jin, *International Journal of Hydrogen Energy*, 2023, **48**, 16593-16600.
9. T. Bhowmik, M. K. Kundu and S. Barman, *Acs Catalysis*, 2016, **6**, 1929-1941.

10. P. Wang, K. Jiang, G. Wang, J. Yao and X. Huang, *Angewandte Chemie*, 2016, **128**, 13051-13055.
11. Q. Lu, A.-L. Wang, Y. Gong, W. Hao, H. Cheng, J. Chen, B. Li, N. Yang, W. Niu and J. Wang, *Nature chemistry*, 2018, **10**, 456-461.
12. Q. Lu, A. L. Wang, H. Cheng, Y. Gong, Q. Yun, N. Yang, B. Li, B. Chen, Q. Zhang and Y. Zong, *Small*, 2018, **14**, 1801090.
13. T. Zhu, J. Huang, B. Huang, N. Zhang, S. Liu, Q. Yao, S. C. Haw, Y. C. Chang, C. W. Pao and J. M. Chen, *Advanced Energy Materials*, 2020, **10**, 2002860.
14. Y. Zhao, H. Cong, P. Li, D. Wu, S. Chen and W. Luo, *Angewandte Chemie*, 2021, **133**, 7089-7093.
15. Y. Yu, K. Jiang, M. Luo, Y. Zhao, J. Lan, M. Peng, F. M. de Groot and Y. Tan, *ACS nano*, 2021, **15**, 5333-5340.
16. Y. L. Wu, X. Li, Y. S. Wei, Z. Fu, W. Wei, X. T. Wu, Q. L. Zhu and Q. Xu, *Advanced Materials*, 2021, **33**, 2006965.
17. J. Gu, L. Li, Y. Xie, B. Chen, F. Tian, Y. Wang, J. Zhong, J. Shen and J. Lu, *Nature Communications*, 2023, **14**, 5389.
18. Z. Zhang, G. Liu, X. Cui, B. Chen, Y. Zhu, Y. Gong, F. Saleem, S. Xi, Y. Du and A. Borgna, *Advanced Materials*, 2018, **30**, 1801741.
19. X. Yan, L. Tian, M. He and X. Chen, *Nano letters*, 2015, **15**, 6015-6021.
20. H. Xu, J. Wan, H. Zhang, L. Fang, L. Liu, Z. Huang, J. Li, X. Gu and Y. Wang, *Advanced Energy Materials*, 2018, **8**, 1800575.
21. W. Zhang, Y. Zou, H. Liu, S. Chen, X. Wang, H. Zhang, X. She and D. Yang, *Nano Energy*, 2019, **56**, 813-822.
22. L. Zhao, H. Yuan, D. Sun, J. Jia, J. Yu, X. Zhang, X. Liu, H. Liu and W. Zhou, *Nano Energy*, 2020, **77**, 105056.
23. J. Song, Y. Q. Jin, L. Zhang, P. Dong, J. Li, F. Xie, H. Zhang, J. Chen, Y. Jin and H. Meng, *Advanced Energy Materials*, 2021, **11**, 2003511.
24. D. Liu, H. Ai, M. Chen, P. Zhou, B. Li, D. Liu, X. Du, K. H. Lo, K. W. Ng and S. P. Wang, *Small*, 2021, **17**, 2007557.
25. M. Zhou, X. Jiang, W. Kong, H. Li, F. Lu, X. Zhou and Y. Zhang, *Nano-Micro Letters*, 2023, **15**, 166.
26. L. Yang, Z. Guo, J. Huang, Y. Xi, R. Gao, G. Su, W. Wang, L. Cao and B. Dong, *Advanced Materials*, 2017, **29**, 1704574.
27. S. Huang, Y. Meng, Y. Cao, F. Yao, Z. He, X. Wang, H. Pan and M. Wu, *Applied Catalysis B: Environmental*, 2020, **274**, 119120.
28. X. Peng, A. M. Qasim, W. Jin, L. Wang, L. Hu, Y. Miao, W. Li, Y. Li, Z. Liu and K. Huo, *Nano Energy*, 2018, **53**, 66-73.
29. X. Li, L. Xiao, L. Zhou, Q. Xu, J. Weng, J. Xu and B. Liu, *Angewandte Chemie*, 2020, **132**, 21292-21299.
30. N. Chen, Y.-X. Du, G. Zhang, W.-T. Lu and F.-F. Cao, *Nano Energy*, 2021, **81**, 105605.
31. W. Tang, S. Zhu, H. Jiang, Y. Liang, Z. Li, S. Wu and Z. Cui, *Journal of Colloid and Interface Science*, 2022, **625**, 606-613.
32. W. Chen, J. Pei, C. T. He, J. Wan, H. Ren, Y. Zhu, Y. Wang, J. Dong, S. Tian and W. C. Cheong, *Angewandte Chemie*, 2017, **129**, 16302-16306.
33. Z.-J. Chen, G.-X. Cao, L.-Y. Gan, H. Dai, N. Xu, M.-J. Zang, H.-B. Dai, H. Wu and P. Wang, *Acs Catalysis*, 2018, **8**, 8866-8872.
34. W. Chen, J. Pei, C. T. He, J. Wan, H. Ren, Y. Wang, J. Dong, K. Wu, W. C. Cheong and J. Mao, *Advanced Materials*, 2018, **30**, 1800396.
35. L. Cao, Q. Luo, W. Liu, Y. Lin, X. Liu, Y. Cao, W. Zhang, Y. Wu, J. Yang and T. Yao, *Nature Catalysis*, 2019, **2**, 134-141.

36. X. Liu, L. Zheng, C. Han, H. Zong, G. Yang, S. Lin, A. Kumar, A. R. Jadhav, N. Q. Tran and Y. Hwang, *Advanced Functional Materials*, 2021, **31**, 2100547.
37. L. Wang, X. Liu, L. Cao, W. Zhang, T. Chen, Y. Lin, H. Wang, Y. Wang and T. Yao, *The Journal of Physical Chemistry Letters*, 2020, **11**, 6691-6696.
38. S. Fang, X. Zhu, X. Liu, J. Gu, W. Liu, D. Wang, W. Zhang, Y. Lin, J. Lu and S. Wei, *Nature communications*, 2020, **11**, 1-8.
39. K. L. Zhou, Z. Wang, C. B. Han, X. Ke, C. Wang, Y. Jin, Q. Zhang, J. Liu, H. Wang and H. Yan, *Nature Communications*, 2021, **12**, 1-10.
40. D. Wang, Q. Li, C. Han, Z. Xing and X. Yang, *Applied Catalysis B: Environmental*, 2019, **249**, 91-97.
41. C. H. Chen, D. Wu, Z. Li, R. Zhang, C. G. Kuai, X. R. Zhao, C. K. Dong, S. Z. Qiao, H. Liu and X. W. Du, *Advanced Energy Materials*, 2019, **9**, 1803913.
42. M. Gong, W. Zhou, M.-C. Tsai, J. Zhou, M. Guan, M.-C. Lin, B. Zhang, Y. Hu, D.-Y. Wang and J. Yang, *Nature communications*, 2014, **5**, 4695.
43. M. Kuang, P. Han, Q. Wang, J. Li and G. Zheng, *Advanced Functional Materials*, 2016, **26**, 8555-8561.
44. B. Zhang, J. Liu, J. Wang, Y. Ruan, X. Ji, K. Xu, C. Chen, H. Wan, L. Miao and J. Jiang, *Nano Energy*, 2017, **37**, 74-80.
45. X. Jin, J. Li, Y. Cui, X. Liu, X. Zhang, J. Yao and B. Liu, *Inorganic Chemistry*, 2019, **58**, 11630-11635.
46. Y. Yu, Z. Dong, L. Tan, N. He, R. Tang, F. Jiang and H. Chen, *Journal of Colloid and Interface Science*, 2022, **611**, 554-563.
47. Y. Tian, M. Wen, A. Huang, Q. Wu, Z. Wang, Q. Zhu, T. Zhou and Y. Fu, *Small*, 2023, 2207569.
48. T. Luo, J. Huang, Y. Hu, C. Yuan, J. Chen, L. Cao, K. Kajiyoshi, Y. Liu, Y. Zhao and Z. Li, *Advanced Functional Materials*, 2023, **33**, 2213058.
49. S. Hong, J. H. Kim, D. Shin, G. Bak, D. Jang, W. B. Kim and Y. J. Hwang, *Applied Surface Science*, 2023, **610**, 155523.
50. M. Liu, Z. Zhang, F. Okejiri, S. Yang, S. Zhou and S. Dai, *Advanced Materials Interfaces*, 2019, **6**, 1900015.
51. R. Q. Yao, Y. T. Zhou, H. Shi, W. B. Wan, Q. H. Zhang, L. Gu, Y. F. Zhu, Z. Wen, X. Y. Lang and Q. Jiang, *Advanced Functional Materials*, 2020, 2009613.
52. Z. Jia, T. Yang, L. Sun, Y. Zhao, W. Li, J. Luan, F. Lyu, L. C. Zhang, J. J. Kruzic and J. J. Kai, *Advanced Materials*, 2020, **32**, 2000385.
53. Z. Jia, K. Nomoto, Q. Wang, C. Kong, L. Sun, L. C. Zhang, S. X. Liang, J. Lu and J. J. Kruzic, *Advanced Functional Materials*, 2021, 2101586.
54. S. Wang, B. Xu, W. Huo, H. Feng, X. Zhou, F. Fang, Z. Xie, J. K. Shang and J. Jiang, *Applied Catalysis B: Environmental*, 2022, **313**, 121472.
55. Z. Jia, Y. Yang, Q. Wang, C. Kong, Y. Yao, Q. Wang, L. Sun, B. Shen and J. J. Kruzic, *ACS Materials Letters*, 2022, **4**, 1389-1396.
56. X. Zhang, Y. Yang, Y. Liu, Z. Jia, Q. Wang, L. Sun, L. C. Zhang, J. J. Kruzic, J. Lu and B. Shen, *Advanced Materials*, 2023, 2303439.
57. Y. Wang, N. Gong, H. Liu, W. Ma, K. Hippalgaonkar, Z. Liu and Y. Huang, *Advanced Materials*, 2023, 2302067.